Available online at www.sciencedirect.com
ScienceDirect
Comput. Methods Appl. Mech. Engrg. 370 (2020) 112976
Computer methods in applied mechanics and engineering
www.elsevier.com/locate/cma

Adaptive multi-material topology optimization with hyperelastic materials under large deformations: A virtual element approach

Xiaojia Shelly Zhang[a,b,*], Heng Chi[c], Glaucio H. Paulino[d]

[a] Department of Civil and Environmental Engineering, University of Illinois, Urbana – Champaign, Urbana, IL 61801, USA
[b] Department of Mechanical Science and Engineering, University of Illinois, Urbana – Champaign, Urbana, IL 61801, USA
[c] Siemens Corporate Technology, 755 College Rd E, Princeton, NJ 08540, USA
[d] School of Civil and Environmental Engineering, Georgia Institute of Technology, 790 Atlantic Drive, Atlanta, GA 30332-0355, USA

Received 30 June 2019; received in revised form 28 February 2020; accepted 1 March 2020
Available online 30 July 2020

Dedicated to the memory of Dr. Joakim Petersson (1968–2002)

Abstract

We introduce a general multi-material topology optimization framework for large deformation problems that effectively handles an arbitrary number of candidate hyperelastic materials and addresses three major associated challenges: material interpolation, excessive distortion of low-density elements, and computational efficiency. To account for many nonlinear elastic materials, we propose a material interpolation scheme that, instead of interpolating multiple material parameters (such as Young's modulus), interpolates multiple nonlinear stored-energy functions. To circumvent convergence difficulties caused by excessive distortions of low-density elements under large deformations, an energy interpolation scheme is revisited to account for multiple candidate hyperelastic materials. Computational efficiency is addressed from both structural analysis and optimization perspectives. To solve the nonlinear state equations efficiently, we employ the lower-order Virtual Element Method in conjunction with tailored adaptive mesh refinement and coarsening strategies. To efficiently update the design variables of the multi-material system, we exploit the separable nature and improve the ZPR (Zhang–Paulino–Ramos) update scheme to account for positive sensitivities and update the design variables associated with each volume constraint in parallel. Four design examples with three types of nonlinear material models demonstrate the efficiency and effectiveness of the proposed framework.

Keywords: Multi-material topology optimization; Hyperelastic materials; Large deformations; ZPR update scheme; Virtual Element Method (VEM); Adaptive refinement and coarsening

1. Introduction

Joakim Petersson contributed to establishing a solid basis for computational topology optimization [1]. He made several important contributions, including techniques to treat numerical instabilities such as checkerboards, mesh-dependence and local minima occurring in topology optimization [2], regularization of intermediate densities [3],

* Corresponding author at: Department of Civil and Environmental Engineering, University of Illinois, Urbana – Champaign, Urbana, IL 61801, USA.
E-mail address: zhangxs@illinois.edu (X.S. Zhang).

https://doi.org/10.1016/j.cma.2020.112976
0045-7825/

and topoloy design for fluid flow [4]. Frequently, he worked at the interface of different fields [1]. Inspired by his contributions and his appreciation of the interconnection of different fields, we propose a general virtual element based topology optimization framework for designing structures composed of multiple hyperelastic materials. The contributions of our proposed framework are as follows. First, a material interpolation scheme is proposed to interpolate an arbitrary number of stored-energy functions of various types. Similarly to the Discrete Material Optimization (DMO) [5], the proposed material interpolation scheme uses a sequence of products among the design variables associated with different materials to effectively penalize material mixture in the final design. We demonstrate three nonlinear material models, which are the modified Saint Venant-Kirchhoff model, the compressible Ogden model, and porous elastomers with Neo-Hookean matrix. Second, to tackle excessive distortions in low-density elements, we adopt the energy interpolation scheme by Wang et al. [6] and extend it to account for multiple candidate materials. With this approach, instead of considering the low-density elements as hyperelastic, the energy interpolation scheme treats them as linear elastic and scales down the level of deformation in those elements. Third, we employ the Virtual Element Method (VEM) for numerical approximation of the finite elasticity boundary value problem, which, in general, leads to fewer function evaluations in forming the multi-material system. Further, since the VEM can easily handle elements of arbitrary shape, it fosters adaptive mesh refinement and coarsening strategies to reduce the size of the state equations without sacrificing design resolution. Additionally, we extend the ZPR design variable update scheme [7] to allow for positive sensitivities while efficiently updating the design variables associated with each volume constraint in parallel.

The ideation of this paper is motivated by the pioneering work of Dr. Joakim Petersson [1]. His work paved the way for many advances in topology optimization, and thus, our multidisciplinary work employing the VEM for nonlinear multimaterial topology optimization is inspired from the work by Petersson [1,2,8,9]. The remainder of this paper is organized as follows. Section 2 elaborates on the three main challenges associated with multi-material topology optimization for problems considering finite deformations and reviews previous attempts in the literature to address them. Section 3 presents both invariant-based and stretch-based isotropic hyperelastic models and reviews the displacement-based variational principle for finite elasticity. Section 4 defines the local displacement virtual element spaces and associated projection operator, and addresses the VEM approximation to the displacement-based variational principle. Section 5 outlines the VEM-based topology optimization considering an arbitrary number of candidate hyperelastic materials emphasizing the treatment of the material and energy interpolations schemes. Section 6 revisits the ZPR design update scheme and introduces a modification to allow for positive sensitivities. Section 7 introduces mesh refinement and coarsening strategies, tailored for the proposed framework, together with a description of the design variable mapping used here. Section 8 presents four numerical examples, highlighting the effectiveness and efficiency of the proposed framework in various design scenarios with combinations of different hyperelastic materials. Section 9 contains concluding remarks. An Appendix complements the paper, which presents a Finite Element (FE) approximation of the potential energy of the multi-material system and discusses the comparison between the virtual element and FE approximations.

2. Challenges and related work

Several approaches exist in the literature for multi-material topology optimization, such as density-based [5,10–16], level set [17–21], phase field [22–24], moving morphable component [25], and the ground structure [7,26] methods. This paper focuses on the density-based approach. While most of the work in multi-material topology optimization employs multiple linear elastic materials, less attention has been paid to the consideration of multiple nonlinear elastic materials under large deformations, which are typical in real-world applications (see, however, [7, 22,26,27] for several attempts in the continuum and discrete element settings). Incorporating multiple nonlinear elastic materials into topology optimization presents three major challenges: material interpolation, excessive distortion of low-density elements, and computational cost. In the following, we elaborate on these challenges and summarize previous attempts in addressing them, before detailing our general VEM-based multi-material topology optimization framework for nonlinear elastic structures.

2.1. Material interpolation

Most material interpolation schemes in multi-material topology optimization account for multiple linear elastic materials. For example, the Solid Isotropic Material with Penalization (SIMP) [28] scheme is generalized in [10,11]

to three-phase materials (two material phases plus one void phase) and in [12] to an arbitrary number of material phases. Another popular material interpolation scheme that can also handle an arbitrary number of material phases is the DMO [5], which introduces a product rule to penalize material mixture. Because the behavior of a linear elastic material is independent of deformation, the aforementioned material interpolation schemes only need to interpolate material parameters such as Young's modulus (or modulus tensors in the anisotropic cases). However, these schemes become limited when considering multiple nonlinear elastic materials because their behavior is typically characterized by a stored-energy function, which is a nonlinear function of deformation [29]. Thus, accounting for multiple nonlinear elastic materials requires a material interpolation scheme capable of effectively interpolating multiple stored-energy functions (possibly of different forms). To achieve this goal, we propose a DMO-type material interpolation scheme that is capable of interpolating an arbitrary number of stored-energy functions of various types.

2.2. Excessive distortion of low-density elements

In the literature, various techniques have been proposed to alleviate convergence difficulties caused by the excessive distortion of low-density elements, (see [6,30–35] for an incomplete sample). For instance, Yoon and Kim [31] introduced an element connectivity parametrization to overcome numerical instability of low-density elements. In their approach, the structural topology is parametrized by a set of zero length elastic links and, instead of optimizing the density of the finite element, the density of the link is optimized. Wang et al. [6] proposed an energy interpolation scheme to stabilize numerical instability of low-density elements by using the element densities to interpolate between the actual stored-energy function and the one of linear elasticity. For solid elements, the actual stored-energy function is used and, for low-density elements, the stored-energy function of linear elasticity is employed. Van Dijk et al. [33] suggested a deformation scaling technique to scale down the level of deformation in low-density elements. Luo et al. [34] presented an additive hyperelastic technique that is able to alleviate the excessive deformation and instability of the low-density elements. The aforementioned studies have demonstrated varying degrees of success in addressing excessive distortions of low-density elements in a single material setting. In this work, we adopt the energy interpolation scheme proposed by Wang et al. [6] and extend it to account for multiple candidate materials.

2.3. Computational efficiency: solution of the state equation

In terms of the structural analysis, topology optimization considering large deformations is computationally expensive because the nonlinear state equation needs to be solved iteratively at every optimization step. Additionally, accounting for multiple nonlinear elastic materials exacerbates the expense of computation because, in order to form the system of nonlinear state equations, the nonlinear response of each material has to be evaluated. A common approach to improve the computational efficiency of topology optimization without sacrificing design resolution and accuracy is to adaptively refine and coarsen the mesh. However, most existing work in topology optimization focuses on adaptive mesh refinement and linear material behavior (see, e.g., [36–40] for single material and [41] for multi-material topology optimization) and relatively little attention has been paid to adaptive mesh coarsening and nonlinearities in material and geometry. To improve the computational efficiency in the structural analysis, this work proposes a tailored adaptive mesh refinement and coarsening strategy that is enabled by the VEM used to approximate the boundary value problem of finite elasticity. The VEM has been successfully applied in many problems in structural mechanics, such as linear elasticity [42–45], small deformation nonlinear elasticity and inelasticity [46–49], finite elasticity [50,51] and elasto-plasticity [52], plate bending [53–56], contact mechanics [57], and fracture mechanics [58,59]. The VEM has also been applied to single and multiple material topology optimization problems considering small deformations [60–63].

2.4. Computational efficiency: nonlinear optimization

Multi-material topology optimization naturally involves multiple design variable fields and typically consists of multiple volume constraints. As a result, the efficient Optimality Criteria (OC) method [64], introduced specifically for compliance-minimization problems with a single volume constraint, is no longer applicable. One approach is to

use the general-purpose Method of Moving Asymptotes (MMA) [65], in which the design variables are updated in a coupled way with respect to all the constraints. Alternatively, an active-phase algorithm, introduced in [24] and further studied in references [66,67], performs sequential binary updates of the material phases; however, is limited to linear elastic materials because it requires the arrangement of the candidate materials in sequence according to stiffness. In [7], a tailored design update scheme, named Zhang–Paulino–Ramos (ZPR), was proposed for multi-material topology optimization to handle both nonlinear [7,26] and linear [15,68] candidate materials and to update the design variables associated with each volume constraint independently (e.g., in parallel). The ZPR design update scheme is employed in this work to efficiently update the design variables in parallel, and is modified to handle both positive and negative sensitivities.

3. Finite elasticity and hyperelastic material models

Consider an isotropic elastic solid $\Omega \in \mathbb{R}^d$ of dimension d. On the boundary, the solid is subjected to a prescribed displacement $\mathbf{u}^0$ on $\Gamma^{\mathbf{X}}$ and a prescribed traction $\mathbf{t}$ on $\Gamma^{\mathbf{t}}$, such that $\Gamma^{\mathbf{X}} \cup \Gamma^{\mathbf{t}} = \partial\Omega$ and $\Gamma^{\mathbf{X}} \cap \Gamma^{\mathbf{t}} = \emptyset$. In the remainder of this section, we introduce three constitutive models for hyperelastic materials in conjunction with the displacement-based variational principle for solving finite elasticity boundary value problems. Throughout this work, we adopt a Lagrangian description of the solid and neglect body forces.

3.1. Hyperelastic constitutive models for isotropic solids

In hyperelasticity, the constitutive behavior of the solid is characterized by a stored-energy function W. To ensure objectivity, the stored-energy function W only depends on the right Cauchy–Green deformation tensor $\mathbf{C} = \mathbf{F}^T\mathbf{F}$, namely, $W(\mathbf{X}, \mathbf{C})$, where $\mathbf{X}$ is the position vector in the undeformed configuration and $\mathbf{F}$ is the deformation gradient tensor. We adopt the second Piola–Kirchoff stress measure, which is given by

$$\mathbf{S} = 2\frac{\partial W}{\partial \mathbf{C}}(\mathbf{X}, \mathbf{C}). \tag{1}$$

Constitutive models in terms of invariants. For isotropic solids, the stored-energy function W depends on $\mathbf{C}$ through its invariants I_1, I_2, and J, which are given by

$$I_1 = \mathrm{tr}\mathbf{C} \quad I_2 = \mathrm{tr}(\mathbf{C}^2) \quad J = \sqrt{\det \mathbf{C}}. \tag{2}$$

We use ϕ to denote the form of the stored energy function expressed in terms of the three invariants, namely, $\phi(\mathbf{X}, I_1, I_2, J) = W(\mathbf{X}, \mathbf{C})$. In this case, the second Piola–Kirchoff stress can be expressed as

$$\mathbf{S} = 2\Big(\frac{\partial \phi}{\partial I_1}\frac{\partial I_1}{\partial \mathbf{C}} + \frac{\partial \phi}{\partial I_2}\frac{\partial I_2}{\partial \mathbf{C}} + \frac{\partial \phi}{\partial J}\frac{\partial J}{\partial \mathbf{C}}\Big) = 2\Big(\frac{\partial \phi}{\partial I_1}\mathbf{I} + 2\frac{\partial \phi}{\partial I_2}\mathbf{C} + \frac{J}{2}\frac{\partial \phi}{\partial J}\mathbf{C}^{-1}\Big). \tag{3}$$

The Lagrangian elasticity tensor, $\mathbb{C} = 4\partial^2\phi/\partial\mathbf{C}\partial\mathbf{C}$, can be obtained in a similar manner to the second Piola–Kirchoff stress. Its expression is not provided here for brevity, but can be found in [69].

This work contains three hyperelastic models. For the model in terms of invariants, we consider the modified Saint Venant-Kirchhoff model [70], which is given by

$$\boxed{\phi(I_1, I_2, J) = \frac{\mu}{4}(I_1^2 - 2I_2 - 2I_1 + 3) + \frac{\lambda}{2}(J-1)^2}, \tag{4}$$

where λ and μ are the first Lame's constant and the shear modulus, respectively.

Constitutive models in terms of principal stretches. Stored-energy functions are often expressed in terms of principal stretches λ_1, λ_2, and λ_3 as

$$\Psi(\mathbf{X}, \lambda_1, \lambda_2, \lambda_3) = W(\mathbf{X}, \mathbf{C}). \tag{5}$$

With the principal stretches, the right Cauchy–Green deformation tensor can be expressed in spectral form as

$$\mathbf{C} = \sum_{\alpha=1}^{3} \lambda_\alpha^2 \mathbf{N}^\alpha \otimes \mathbf{N}^\alpha, \tag{6}$$

where $\mathbf{N}^\alpha$ is the principal direction associated with λ_α in the undeformed configuration.

For isotropic solids, the second Piola–Kirchoff stress is co-axial with the right Cauchy–Green deformation tensor and can be expressed in the following spectral form:

$$\mathbf{S} = \sum_{\alpha=1}^{3} S_{\alpha\alpha}\mathbf{N}^{\alpha}\otimes\mathbf{N}^{\alpha} = 2\sum_{\alpha=1}^{3}\frac{\partial\Psi}{\partial\lambda_{\alpha}^{2}}\mathbf{N}^{\alpha}\otimes\mathbf{N}^{\alpha}. \tag{7}$$

In addition, the Lagrangian elasticity tensor is given in terms of the principal stretches as

$$\begin{aligned}\mathbb{C} = 4\frac{\partial^{2}W}{\partial\mathbf{C}\partial\mathbf{C}} = 4\Bigg[&\sum_{\alpha=1}^{3}\sum_{\beta=1}^{3}\frac{\partial^{2}\Psi}{\partial\lambda_{\alpha}^{2}\partial\lambda_{\beta}^{2}}\mathbf{N}^{\alpha}\otimes\mathbf{N}^{\alpha}\otimes\mathbf{N}^{\beta}\otimes\mathbf{N}^{\beta}\\ &+\sum_{\substack{\alpha,\beta=1\\ \alpha\neq\beta}}\frac{S_{\alpha\alpha}-S_{\beta\beta}}{\lambda_{\alpha}^{2}-\lambda_{\beta}^{2}}\left(\mathbf{N}^{\alpha}\otimes\mathbf{N}^{\beta}\otimes\mathbf{N}^{\alpha}\otimes\mathbf{N}^{\beta}+\mathbf{N}^{\alpha}\otimes\mathbf{N}^{\beta}\otimes\mathbf{N}^{\beta}\otimes\mathbf{N}^{\alpha}\right)\Bigg].\end{aligned} \tag{8}$$

In the special case of $\lambda_{\alpha}=\lambda_{\beta}$, the ratio in the second term of the above expression is replaced by the limit

$$\lim_{\lambda_{\beta}\to\lambda_{\alpha}}\frac{S_{\alpha\alpha}-S_{\beta\beta}}{\lambda_{\alpha}^{2}-\lambda_{\beta}^{2}} = 2\left(\frac{\partial^{2}\Psi}{\partial\lambda_{\beta}^{2}\lambda_{\beta}^{2}}-\frac{\partial^{2}\Psi}{\partial\lambda_{\alpha}^{2}\lambda_{\beta}^{2}}\right). \tag{9}$$

A representative example of the stored-energy function expressed in terms of principal stretches is the Ogden model [71], which is commonly used to model elastomers and soft tissues. In this work, the second type of hyperelastic models is the *compressible Ogden model* [72], adopted as follows:

$$\boxed{\Psi(\lambda_1,\lambda_2,\lambda_3) = \sum_{a=1}^{N_O}\left[\frac{\mu_a}{m_a^2}\left(\lambda_1^{m_a}+\lambda_2^{m_a}+\lambda_3^{m_a}-3\right)-\frac{\mu_a}{m_a}\ln(\lambda_1\lambda_2\lambda_3)\right]+\frac{\kappa}{2}\left(\lambda_1\lambda_2\lambda_3-1\right)^{2}}, \tag{10}$$

where $\mu_a\in\mathbb{R}_+$ and $m_a\in\mathbb{R}$ are parameters, N_O is the number of terms, and κ is the bulk modulus. Based on the material parameters, the shear modulus is given by $\mu=\sum_{a=1}^{N_O}\mu_a/2$. We note that, by varying N_O and m_a, the above Ogden model has great flexibility in controlling the degree of tension–compression asymmetry in the model [72,73].

We emphasize that the proposed multi-material topology optimization framework is general in terms of the material models combination. To demonstrate this flexibility, in addition to the previous two conventional hyperelastic models, we also consider a stored-energy function for 2D porous elastomers with *incompressible Neo-Hookean matrix* under the plane strain condition (i.e., $\lambda_3=1$) derived from the homogenization theory [74], which takes the following expression,

$$\boxed{\Psi(\lambda_1,\lambda_2,1) = \frac{\mu}{2}\frac{1-f_0}{1+f_0}\left(\lambda_1^{2}+\lambda_2^{2}-2\lambda_1\lambda_2\right)+\frac{\mu}{2}\left(\lambda_1\lambda_2-2\right)\log\left(\frac{\lambda_1\lambda_2+f_0-1}{f_0\lambda_1\lambda_2}\right)}, \tag{11}$$

where μ is the shear modulus of the Neo-Hookean matrix and f_0 is the porosity in the undeformed configuration.

3.2. The displacement-based variational principle for finite elasticity

This work focuses on the standard displacement-based formulation, in which the displacement field $\mathbf{v}$ is the only independent field. The deformation gradient $\mathbf{F}$ is then assumed to be a function of $\mathbf{v}$ given by $\mathbf{F}(\mathbf{v})=\mathbf{I}+\nabla\mathbf{v}$, where ∇ stands for the gradient operator with respect to the undeformed configuration and $\mathbf{I}$ denotes the second order identity tensor. Accordingly, the right Cauchy–Green deformation and second Piola–Kirchoff tensors are dependent on $\mathbf{v}$ through $\mathbf{F}$.

The classical principle of minimum potential energy seeks the equilibrating displacement field $\mathbf{u}$, which minimizes the potential energy Π among all the kinematically admissible displacement fields, namely,

$$\Pi(\mathbf{u}) = \min_{\mathbf{v}\in\mathcal{K}}\left\{\int_{\Omega}W(\mathbf{X},\mathbf{C}(\mathbf{v}))\mathrm{d}\mathbf{X}-\int_{\Gamma^{\mathbf{t}}}\mathbf{t}\cdot\mathbf{v}\mathrm{d}S\right\}, \tag{12}$$

where $\mathcal{K}$ stands for the space of kinematically admissible displacement fields. Moreover, the weak form of the above variational principle (12) reads as follows:

$$G(\mathbf{v}, \delta\mathbf{v}) = \int_{\Omega} \Big[\mathbf{F}(\mathbf{v}) \cdot \mathbf{S}(\mathbf{X}, \mathbf{v})\Big] : \nabla(\delta\mathbf{v}) \mathrm{d}\mathbf{X} - \int_{\Gamma^{\mathbf{t}}} \mathbf{t} \cdot \delta\mathbf{v} \mathrm{d}S = 0, \quad \forall \delta\mathbf{v} \in \mathcal{K}_0, \tag{13}$$

where $\delta\mathbf{v}$ is the variation of $\mathbf{v}$ and $\mathcal{K}_0$ denotes the set of kinematically admissible displacements, which vanish on $\Gamma^{\mathbf{X}}$. In absence of deformation-dependent traction, the linearized weak form is given by

$$G(\mathbf{v}, \delta\mathbf{v}) + DG(\mathbf{v}, \delta\mathbf{v}) \cdot \mathbf{w} = 0 \quad \forall \delta\mathbf{v} \in \mathcal{K}_0, \tag{14}$$

with

$$DG(\mathbf{v}, \delta\mathbf{v}) \cdot \mathbf{w} = \int_{\Omega} \nabla\mathbf{w} : \mathbb{L}(\mathbf{X}, \mathbf{v}) : \nabla\delta\mathbf{v} \mathrm{d}\mathbf{x}. \tag{15}$$

In the above expression, the modulus $\mathbb{L}$, expressed in indicial notation, is

$$L_{iJkL}(\mathbf{X}, \mathbf{v}) = \delta_{ik} S_{JL}(\mathbf{X}, \mathbf{v}) + F_{iN}(\mathbf{v}) F_{kM}(\mathbf{v}) C_{NJML}(\mathbf{X}, \mathbf{v}), \tag{16}$$

where S_{JL}, F_{iN}, and C_{NJML} are the components of $\mathbf{S}$, $\mathbf{F}$, and $\mathbb{C}$, respectively; and δ_{ik} is the Kronecker delta.

For hyperelastic models given in terms of principal stretches, by plugging the expressions of $\mathbf{S}$ and $\mathbb{C}$ in terms of the principal stretches into (16), we obtain the expression of $\mathbb{L}$ in terms of λ_1, λ_2, and λ_3 as

$$\begin{aligned}\mathbb{L} = {} & 2\sum_{\alpha=1}^{3}\sum_{\beta=1}^{3} \frac{\partial \Psi}{\partial \lambda_\alpha^2} \mathbf{n}^\beta \otimes \mathbf{N}^\alpha \otimes \mathbf{n}^\beta \otimes \mathbf{N}^\alpha + 4\sum_{\alpha=1}^{3}\sum_{\beta=1}^{3} \lambda_\alpha \lambda_\beta \frac{\partial^2 \Psi}{\partial \lambda_\alpha^2 \partial \lambda_\beta^2} \mathbf{n}^\alpha \otimes \mathbf{N}^\alpha \otimes \mathbf{n}^\beta \otimes \mathbf{N}^\beta \\ & + 4 \sum_{\substack{\alpha,\beta=1 \\ \alpha \neq \beta}} \frac{S_{\alpha\alpha} - S_{\beta\beta}}{\lambda_\alpha^2 - \lambda_\beta^2} \Big(\lambda_\alpha^2 \mathbf{n}^\alpha \otimes \mathbf{N}^\beta \otimes \mathbf{n}^\alpha \otimes \mathbf{N}^\beta + \lambda_\alpha \lambda_\beta \mathbf{n}^\alpha \otimes \mathbf{N}^\beta \otimes \mathbf{n}^\beta \otimes \mathbf{N}^\alpha \Big),\end{aligned} \tag{17}$$

where $\mathbf{n}^\alpha \doteq \mathbf{F}\mathbf{N}^\alpha / \lambda_{\lambda_\alpha}$ is the unit vector in the deformed configuration.

4. VEM space, projection, and approximation

This section introduces the local virtual element space for the displacement field and addresses the VEM approximation to the continuum variational principle (12) in 2D [75]. In particular, the basic definition of a 2D linear virtual element space is defined and a projection operator, which maps functions in the local space onto linear ones, is introduced. Throughout the section, we comply with the following conventions. For a given tessellation Ω_h that discretizes the domain Ω into non-overlapping polygons, we denote E and e as its generic element and edge, respectively. Moreover, we use $|E|$ and $|e|$ to denote the area of E and length of e, respectively.

4.1. Local VEM space and projection operator

Given a polygon E with n vertices, we assume that its vertices are numbered in a counterclockwise fashion as, $\mathbf{X}_i = [X_i, Y_i]^T$, $i = 1, \ldots, n$. We then define the local virtual element space $\mathcal{V}(E)$ as [75]:

$$\mathcal{V}(E) = \left\{ v \in \mathcal{H}^1(E) : v|_e \in \mathcal{P}_1(E) \ \forall e \in E \text{ and } \Delta v = 0 \text{ in } E \right\}, \tag{18}$$

where Δ stands for the Laplacian operator and $\mathcal{P}_1(\cdot)$ is the space of linear functions. According to the above definition, the local space $\mathcal{V}(E)$ contains functions that are harmonic in the interior of the E and have piecewise linear variations on the boundary of E. We can show that $\mathcal{V}(E)$ is linearly complete, namely, $\mathcal{P}_1(E) \in \mathcal{V}(E)$, and its degrees of freedom (DOFs) are the values of its functions at the vertices of E [75].

Although any given function v in $\mathcal{V}(E)$ is only known implicitly in the interior of E, we can exactly compute the average gradient of v over E with the DOFs of v and geometric information of E. In fact, using integration by parts, we have the following relation:

$$\frac{1}{|E|} \int_E \nabla v \mathrm{d}\mathbf{X} = \frac{1}{|E|} \int_{\partial E} v \mathbf{N} \mathrm{d}S = \frac{1}{|E|} \sum_{e \in \partial E} \int_e v \, \mathbf{N}_e \mathrm{d}S. \tag{19}$$

Realizing that v varies piecewise-linearly on ∂E, we arrive at

$$\frac{1}{|E|}\int_E \nabla v \, \mathrm{d}\mathbf{X} = \frac{1}{2|E|}\sum_{i=1}^{n} v(\mathbf{X}_i)\left(|e_i|\mathbf{N}_{e_i} + |e_{i-1}|\mathbf{N}_{e_{i-1}}\right), \tag{20}$$

where $|e_i|$ and $\mathbf{N}_{e_i}$ are the length and the outward normal vector of edge e_i, respectively; and the conventions, $i+1=1$ when $i=n$, and $i-1=n$ when $i=1$, are used in the above summation.

By definition of $\mathcal{V}(E)$, the function v is known explicitly on the boundary, but only implicitly defined in the interior of element domain E. In order to construct the VEM approximation to the variational principle with $\mathcal{V}(E)$, we make use of a projection operator, Π_E^{∇}, which maps functions in $\mathcal{V}(E)$ onto the space of linear functions $\mathcal{P}_1(E)$. For any given $v \in \mathcal{V}(E)$, the projection $\Pi_E^{\nabla} v$ is formally defined by the following two conditions,

$$\int_E \nabla(\Pi_E^{\nabla} v)\cdot\nabla p_1 \mathrm{d}\mathbf{X} = \int_E \nabla v : \nabla p_1 \mathrm{d}\mathbf{X} \quad \forall p_1 \in \mathcal{P}_1(E) \quad \text{and} \quad \sum_{i=1}^{m} v(\mathbf{X}_i) = \sum_{i=1}^{m} \Pi_E^{\nabla} v(\mathbf{X}_i), \tag{21}$$

where we recall that $\mathbf{X}_i$ is the ith vertex of E. Because both $\nabla(\Pi_E^{\nabla} v)$ and ∇p_1 are constant vectors, the first condition in (21) can be recast as

$$\nabla(\Pi_E^{\nabla} v) = \frac{1}{|E|}\int_E \nabla v \mathrm{d}\mathbf{X}. \tag{22}$$

According to (20), the right-hand side of (22) is exactly computable with only the DOFs of v and geometric information of E. Once $1/|E|\int_E \nabla v \mathrm{d}\mathbf{X}$ is obtained, the projection $\Pi_E^{\nabla} v$ can be exactly computed using this value together with the second condition in (21), which essentially fixes the constant term of the linear function.

4.2. Displacement-based VEM approximation for finite elasticity

Having defined the VEM local space and the projection operator, this subsection addresses the virtual element approximation of the continuum variational principle (12). For a tessellation Ω_h of the domain Ω, which consists of non-overlapping elements, we assume that the boundary of the mesh Γ_h is compatible with the applied displacement and traction boundary conditions, that is, both $\Gamma_h^{\mathbf{X}}$ and $\Gamma_h^{\mathbf{t}}$ are unions of the edges in the mesh.

We first state the global displacement space, denoted by $\mathcal{K}_h$, as

$$\mathcal{K}_h \doteq \left\{\mathbf{v}_h \in \mathcal{K} : \mathbf{v}_h|_E \in [\mathcal{V}(E)]^2, \ \forall E \in \Omega_h\right\}. \tag{23}$$

According to the global displacement space, the local displacement field $\mathbf{v} = [v_x, v_y]^T$ within each element exists in the local virtual element space $[\mathcal{V}(E)]^2$. We also use $\mathbf{\Pi}_E^{\nabla}\mathbf{v}$ to denote the projection of the displacement in element E as $\mathbf{\Pi}_E^{\nabla}\mathbf{v} = [\Pi_E^{\nabla} v_x, \Pi_E^{\nabla} v_y]^T$. According to (22), we have

$$\nabla(\mathbf{\Pi}_E^{\nabla}\mathbf{v}) = \frac{1}{|E|}\int_E \nabla\mathbf{v}\mathrm{d}\mathbf{X}. \tag{24}$$

With the aforementioned notations, we now proceed to the construction of the VEM approximation for the continuous variational principle of finite elasticity problems. As a first step, we decompose the domain integral into the summation of element-level contributions as

$$\Pi_h(\mathbf{v}_h) = \sum_{E\in\Omega_h}\int_E W(\mathbf{C}(\mathbf{v}_h))\mathrm{d}\mathbf{X} - \int_{\Gamma_h^{\mathbf{t}}} \mathbf{t}_h\cdot\mathbf{v}_h \mathrm{d}S. \tag{25}$$

To construct the VEM approximation of $\Pi_h(\mathbf{v}_h)$, which will be denoted as $\Pi_h^{VEM}(\mathbf{v}_h)$, we then need to approximate the internal energy of each element E. Following the VEM philosophy, we approximate the internal energy of each element using the decomposition as

$$\int_E W\Big(\mathbf{C}(\mathbf{v}_h)\Big)\mathrm{d}\mathbf{X} \approx |E| W\Big(\mathbf{C}(\mathbf{\Pi}_E^{\nabla}\mathbf{v}_h)\Big) + \frac{1}{2}\alpha_E(\mathbf{\Pi}_E^{\nabla}\mathbf{v}_h) S_{h,E}\Big(\mathbf{v}_h - \mathbf{\Pi}_E^{\nabla}\mathbf{v}_h, \mathbf{v}_h - \mathbf{\Pi}_E^{\nabla}\mathbf{v}_h\Big). \tag{26}$$

The first term on the right-hand side of (26) is commonly known as the consistency term, which only uses the projection of the displacement field. This term is first-order consistent, meaning that, if $\mathbf{v}_h$ is a linear vector field, this term recovers the exact internal energy in element E. The consistent term is not enough to constitute a stable

approximation because it introduces non-physical zero energy modes. Thus, a stability term is needed, which is given by the second term on the right-hand side of (26). The stability term consists of two components, a scalar-valued function $\alpha_E(\boldsymbol{\Pi}_E^{\nabla}\mathbf{v}_h)$ and a bilinear form $S_{h,E}(\cdot,\cdot)$, which is given by [46] as follows,

$$S_{h,E}(\mathbf{v}_h,\mathbf{w}_h)=\sum_{i=1}^{m}\mathbf{v}_h(\mathbf{X}_i)\cdot\mathbf{W}_h(\mathbf{X}_i)\quad\forall\mathbf{v}_h,\mathbf{w}_h\in\mathcal{K}_h, \tag{27}$$

where we recall that $\mathbf{X}_i$ stands for the ith vertex of element E. The explicit expressions of the scalar-valued stability parameter $\alpha_E(\boldsymbol{\Pi}_E^{\nabla}\mathbf{v}_h)$ will be discussed in the next subsection. In terms of the external energy, $\langle\mathbf{t},\mathbf{v}_h\rangle_h$, we adopt the same approximation as the one presented in [50].

We are now ready to introduce the final form of the VEM approximation to the continuous problem (12), which consists of seeking the unknown displacement field $\mathbf{u}_h$ such that

$$\Pi_h^{VEM}(\mathbf{u}_h)=\min_{\mathbf{v}_h\in\mathcal{K}_h}\left\{\sum_E\left[|E|W\Big(\mathbf{C}(\boldsymbol{\Pi}_E^{\nabla}\mathbf{v}_h)\Big)+\frac{1}{2}\alpha_E(\boldsymbol{\Pi}_E^{\nabla}\mathbf{v}_h)S_{h,E}(\mathbf{v}_h-\boldsymbol{\Pi}_E^{\nabla}\mathbf{v}_h,\mathbf{v}_h-\boldsymbol{\Pi}_E^{\nabla}\mathbf{v}_h)\right]-\langle\mathbf{t},\mathbf{v}_h\rangle_h\right\}. \tag{28}$$

Accordingly, the weak form of the VEM approximation (28) takes the following form

$$\begin{aligned}&G_h(\mathbf{v}_h,\delta\mathbf{v}_h)\\&=\sum_E\Big[|E|(\mathbf{I}+\nabla\boldsymbol{\Pi}_E^{\nabla}\mathbf{v}_h)\mathbf{S}(\boldsymbol{\Pi}_E^{\nabla}\mathbf{v}_h)+\frac{1}{2}S_{h,E}\Big(\mathbf{v}_h-\boldsymbol{\Pi}_E^{\nabla}\mathbf{v}_h,\mathbf{v}_h-\boldsymbol{\Pi}_E^{\nabla}\mathbf{v}_h\Big)\frac{\partial\alpha_E}{\partial\mathbf{F}}(\boldsymbol{\Pi}_E^{\nabla}\mathbf{v}_h)\Big]:\nabla\boldsymbol{\Pi}_E^{\nabla}(\delta\mathbf{v}_h)\\&+\sum_E\alpha_E(\boldsymbol{\Pi}_E^{\nabla}\mathbf{v}_h)S_{h,E}\Big(\mathbf{v}_h-\boldsymbol{\Pi}_E^{\nabla}\mathbf{v}_h,\delta\mathbf{v}_h-\boldsymbol{\Pi}_E^{\nabla}(\delta\mathbf{v}_h)\Big)-\langle\mathbf{t},\delta\mathbf{v}_h\rangle_h=0\quad\forall\delta\mathbf{v}_h\in\mathcal{K}_h^0.\end{aligned} \tag{29}$$

In our implementation, the second order information of Π_h^{VEM} [69,76], which is not provided here for the sake of conciseness, is needed in order to use Newton's method.

4.3. Stability parameter $\alpha_E(\cdot)$

The expression for the stability parameter α_E is discussed here and follows the trace-based stabilization strategy proposed in [50]. In a general 2D problem, for a given material model with stored-energy function $W(\mathbf{C})$, the trace-based stability parameter is given by

$$\alpha_E(\boldsymbol{\Pi}_E^{\nabla}\mathbf{s}_h)=\frac{1}{4}\mathrm{tr}\Big(\frac{\partial^2 W}{\partial\mathbf{F}\partial\mathbf{F}}\big(\mathbf{C}(\boldsymbol{\Pi}_E^{\nabla}\mathbf{s}_h)\big)\Big)=\frac{1}{4}\mathrm{tr}\mathbb{L}\Big(\boldsymbol{\Pi}_E^{\nabla}\mathbf{s}_h\Big). \tag{30}$$

where we recall that $\mathbb{L}$ is the modulus defined in (16).

Choice of $\mathbf{s}_h$. In a general setting, $\mathbf{s}_h$ can be taken as any kinematically admissible displacement that does not depend on the loading history.[1] From the several choices of $\mathbf{s}_h$ investigated in reference [50], choosing $\mathbf{s}_h=\mathbf{v}_h$, where $\mathbf{v}_h$ is the displacement field we are seeking, yields the best performance in modeling problems involving large deformation fields. Thus, we use $\mathbf{s}_h=\mathbf{v}_h$ in the present work.

Explicit expressions of α_E. For isotropic materials, explicit expressions of the trace-based stability parameter α_E can be derived, which facilitates a simple implementation. If the stored-energy function ϕ is expressed in terms of the three invariants, I_1, I_2, and J, the explicit expression of α_E for 2D problems is [50]:

$$\begin{aligned}\alpha_E(\boldsymbol{\Pi}_E^{\nabla}\mathbf{s}_h)=\frac{1}{4}\Bigg[&4I_1\frac{\partial^2\phi}{\partial I_1\partial I_1}+(8I_1I_2-4J^2I_1)\frac{\partial^2\phi}{\partial I_2\partial I_2}+I_1\frac{\partial^2\phi}{\partial J\partial J}+16I_2\frac{\partial^2\phi}{\partial I_1\partial I_2}+8J\frac{\partial^2\phi}{\partial I_1\partial J}\\&+2JI_1\frac{\partial^2\phi}{\partial I_2\partial J}+8\frac{\partial\phi}{\partial I_1}+2I_1\frac{\partial\phi}{\partial I_2}\Bigg],\end{aligned} \tag{31}$$

where the dependences of I_1, I_2, and J on $\boldsymbol{\Pi}_E^{\nabla}\mathbf{s}_h$ are assumed.

[1] In topology optimization, we prefer that $\mathbf{s}_h$ be history-independent. A counterexample is choosing $\mathbf{s}_h=\mathbf{v}_h^{n-1}$, where $\mathbf{v}_h^{n-1}$ is the converged displacement solution in the last Newton–Raphson step. If the stability parameter α_E is history dependent, then the sensitivity analysis will become history dependent as well, causing undesirable complication in terms of computational implementation.

We also provide the explicit expression for α_E when the stored-energy function of an isotropic solid is given in terms of the principal stretches. Taking the trace of $\mathbb{L}$ and making use of the following relations,

$$\mathbf{N}^\alpha \cdot \mathbf{N}^\beta = \begin{cases} 1 & \text{if } \alpha = \beta \\ 0 & \text{otherwise} \end{cases} \quad \text{and} \quad \mathbf{n}^\alpha \cdot \mathbf{n}^\beta = \begin{cases} 1 & \text{if } \alpha = \beta \\ 0 & \text{otherwise} \end{cases}, \tag{32}$$

we can simplify the expression of (30) as

$$\boxed{\alpha_E(\boldsymbol{\Pi}_E^\nabla \mathbf{s}_h) = \frac{1}{4}\mathrm{tr}\mathbb{L} = \frac{1}{4}L_{iJiJ} = \frac{1}{4}\left[\sum_{\alpha=1}^{2}\left(2\,S_{\alpha\alpha} + 4\lambda_\alpha^2 \frac{\partial^2 \Psi}{\partial \lambda_\alpha^2 \partial \lambda_\alpha^2}\right) + 4 \sum_{\substack{\alpha,\beta=1 \\ \alpha\neq\beta}}^{2} \frac{S_{\alpha\alpha} - S_{\beta\beta}}{\lambda_\alpha^2 - \lambda_\beta^2}\right]}, \tag{33}$$

where we recall that $S_{\alpha\,\alpha} \doteq 2\partial \Psi/\partial \lambda_\alpha^2$; the dependence of λ_β on $\boldsymbol{\Pi}_E^\nabla \mathbf{s}_h$ is assumed, where $\beta = 1, 2$.

5. VEM-based topology optimization considering multiple hyperelastic materials

Consider a given discretization Ω_h composed of a total of N nodes and M elements. If we further assume that there are a total of m candidate materials, the general topology optimization formulation can be stated as

$$\boxed{\begin{aligned} &\min_{\boldsymbol{\rho}_1,\ldots,\boldsymbol{\rho}_m} \quad J\left(\boldsymbol{\rho}_1,\ldots,\boldsymbol{\rho}_m\right) \\ &\text{s.t.} \quad g^j\left(\boldsymbol{\rho}_1,\ldots,\boldsymbol{\rho}_m\right) = \frac{\sum_{i\in\mathcal{G}^j} \mathbf{V}^T \overline{\boldsymbol{\rho}}_i}{|\Omega_h|} - V^j_{\max} \leq 0, \quad j = 1,\ldots,nc, \\ &\quad \rho_{\min} \leq \rho_i^{(e)} \leq 1, \; i = 1,\ldots,m, \; \text{and } e = 1,\ldots,M, \\ &\text{with } \mathbf{u}_h(\boldsymbol{\rho}_1,\ldots,\boldsymbol{\rho}_m) = \arg\min_{\mathbf{v}_h\in\mathcal{K}_h} \Pi_h^{VEM}(\boldsymbol{\rho}_1,\ldots,\boldsymbol{\rho}_m,\mathbf{v}_h) \end{aligned}} \tag{34}$$

where $J(\cdot)$ is the objective function, $\mathbf{V}$ is the vector of element areas, and $\boldsymbol{\rho}_i$ is the vector of element-wise constant design variables for the ith material with $\rho_i^{(e)}$ the design variable of the eth element. For the jth volume constraint g^j, we denote $\mathcal{G}^j$ as the associated set of material indices and V^j_{max} the associated volume fraction. At every optimization step, the equilibrating displacement is solved by minimizing the VEM approximation of the potential energy of the current design. The VEM approximation of the potential energy Π_h^{VEM} is discussed in Section 5.3, and the particular forms of the objective function $J(\cdot)$ are discussed in Sections 5.4 and 5.5.

In order to regularize the optimization problem, we use a density filter [77]. In formulation (34), we use $\overline{\boldsymbol{\rho}}_i$ to denote the vector of filtered design variables of the ith material through a density filter as

$$\overline{\boldsymbol{\rho}}_i = \mathbf{P}_i \boldsymbol{\rho}_i, \quad i = 1,\ldots,m, \tag{35}$$

where $\mathbf{P}_i$ is the filter matrix corresponding to material i, whose (e,k) component is given as [78]

$$(\mathbf{P}_i)_{e,k} = \frac{\max(0, |E^{(k)}|(1 - |\mathbf{X}_e^c - \mathbf{X}_k^c|/R_i)^q)}{\sum_{k\in S(e)} |E^{(k)}|(1 - |\mathbf{X}_e^c - \mathbf{X}_k^c|/R_i)^q}. \tag{36}$$

We note that, while the prescribed filter radius R_i can be different for each candidate material, we assume the same filter radius R for all the candidate materials in this work. Thus, the density filter matrix $\mathbf{P}_i$ is identical for all the candidate materials and only needs to be formed once.

With the definition of the filtered design variables, we can recast the jth volume constraint $g^j(\boldsymbol{\rho}_1,\ldots,\boldsymbol{\rho}_m)$ as

$$g^j(\boldsymbol{\rho}_1,\ldots,\boldsymbol{\rho}_m) = \frac{\sum_{i\in\mathcal{G}^j} \mathbf{V}^T \mathbf{P}_i \boldsymbol{\rho}_i}{|\Omega_h|} - V^j_{max} = \sum_{i\in\mathcal{G}^j} \overline{\mathbf{V}}_i^T \boldsymbol{\rho}_i - V^j_{max}, \quad j = 1,\ldots,nc, \tag{37}$$

where the vector $\overline{\mathbf{V}}_i$ is introduced such that $\overline{\mathbf{V}}_i \doteq \mathbf{P}_i^T \mathbf{V}/|\Omega_h|$. Componentwise, the eth component of $\overline{\mathbf{V}}_i$ is given by $\overline{V}_i^{(e)} = \sum_k (\mathbf{P}_i)_{k,e} V^{(k)}/|\Omega_h|$. Thus, all the volume constraints are linear with respect to the design variables and their sensitivities are given by

$$\frac{\partial g^j}{\partial \rho_i^{(e)}}(\boldsymbol{\rho}_1,\ldots,\boldsymbol{\rho}_m) = \begin{cases} \overline{V}_i^{(e)} & \text{if } i \in \mathcal{G}^j \\ 0 & \text{otherwise} \end{cases}, \quad j = 1,\ldots,nc. \tag{38}$$

The formulation considering multiple hyperelastic materials under large deformations poses additional challenges: (1) how to define the effective (interpolated) material behavior when there are multiple candidate materials and the nonlinear response of each one is described by its individual stored-energy function; and (2) how to avoid the numerical difficulties associated with the low-density elements, which are typical in topology optimization involving large deformations. In the subsequent subsections, these two issues are addressed in sequence.

5.1. A material interpolation scheme for multiple hyperelastic materials

Unlike the case of optimizing among multiple linear elastic materials, where the interpolation of multiple constant modulus tensors is needed, optimizing among multiple hyperelastic materials requires the interpolation of multiple nonlinear stored-energy functions that may take different forms. We propose a material interpolation scheme that penalizes not only the intermediate densities, but also mixing of multiple materials (i.e., the presence of more than one material at a given location).

Assuming that we have a total of m candidate materials for element (e), and each one is characterized by a stored-energy function W_i, we propose to define the interpolated stored-energy function W^ρ as:

$$W^\rho\big(\rho_1^{(e)},\ldots,\rho_m^{(e)},\mathbf{v}\big)=\sum_{i=1}^{m} w_i(\rho_1^{(e)},\ldots,\rho_m^{(e)})W_i\big(\mathbf{C}(\mathbf{v})\big), \tag{39}$$

where w_i is a weight function associated with the ith candidate material.

In this work, we propose a DMO-type interpolation scheme for multiple hyperelastic candidate materials in which we define the weight function w_i in (39) via the product rule [5] as follows,

$$w_i(\rho_1^{(e)},\ldots,\rho_m^{(e)})=\Big(\overline{\rho}_i^{(e)}\Big)^p\prod_{\substack{j=1\\ j\neq i}}^{m}\Big[1-\Big(\overline{\rho}_j^{(e)}\Big)^p\Big], \tag{40}$$

where $\overline{\rho}_i^{(e)}$ is the filtered density of the eth element associated with the ith candidate material, "$\prod$" is the operator standing for the product of sequence, and p is the SIMP penalization parameter to penalize intermediate densities. We remark that, with this DMO-type material interpolation scheme, the mixture of multiple materials is penalized implicitly through the product rule. For instance, if both materials i and j are solid in element (e) (i.e., $\overline{\rho}_i^{(e)}=\overline{\rho}_j^{(e)}=1$ for any given $i\neq j$), we have $w_k=0$, $k=1,\ldots,m$ according to (40). Thus, element (e) will not have any stored energy even if both materials i and j are present.

Remark 5.1. We can show that the proposed material interpolation scheme reduces to the original DMO interpolation scheme when all the candidate materials are linear elastic. If the ith candidate material is linear elastic, its stored-energy function can be expressed as

$$W_i(\mathbf{v})=\frac{1}{2}\boldsymbol{\varepsilon}(\mathbf{v}):\mathbb{C}_i:\boldsymbol{\varepsilon}(\mathbf{v}), \tag{41}$$

where $\mathbb{C}_i$ is the elasticity modulus tensor. Plugging in the above stored-energy function to the proposed material interpolation scheme (39), we arrive at

$$\begin{aligned} W^\rho(\rho_1^{(e)},\ldots,\rho_m^{(e)},\mathbf{v}) &= \sum_{i=1}^{m} w_i(\rho_1^{(e)},\ldots,\rho_m^{(e)})\frac{1}{2}\boldsymbol{\varepsilon}(\mathbf{v}):\mathbb{C}_i:\boldsymbol{\varepsilon}(\mathbf{v})\\ &= \frac{1}{2}\boldsymbol{\varepsilon}(\mathbf{v}):\Big[\sum_{i=1}^{m} w_i(\rho_1^{(e)},\ldots,\rho_m^{(e)})\mathbb{C}_i\Big]:\boldsymbol{\varepsilon}(\mathbf{v})\\ &= \frac{1}{2}\boldsymbol{\varepsilon}(\mathbf{v}):\mathbb{C}^\rho:\boldsymbol{\varepsilon}(\mathbf{v}). \end{aligned} \tag{42}$$

In the above expression, we note that $\mathbb{C}^\rho\doteq\sum_{i=1}^{m} w_i(\rho_1^{(e)},\ldots,\rho_m^{(e)})\mathbb{C}_i$ is the interpolated elasticity modulus in the original DMO interpolation scheme [5].

5.2. An energy interpolation scheme for low-density elements

For topology optimization problems involving large deformations, elements with low densities become problematic as they undergo excessive distortion. As a consequence, non-convergence of nonlinear solvers may be encountered. To overcome this issue, several techniques have been introduced in the literature for single material topology optimization, see, e.g. [6,30–35].

In this work, we adopt the energy interpolation approach proposed by Wang et al. [6], whose basic idea is to use the actual stored-energy function for elements with high densities and a linear elastic stored-energy function for low-density elements. The original energy interpolation scheme developed in [6] is for the single material case. In this work, we extend it to problems with any number of candidate hyperelastic materials.

With W^{ρ} the true stored-energy function for element (e), whose form is defined in (39), we can define the energy interpolation form of this element as

$$\begin{aligned} W^{\rho,\gamma}\left(\rho_1^{(e)},\dots,\rho_m^{(e)},\gamma^{(e)},\mathbf{v}\right) = {} & W^{\rho}\left(\rho_1^{(e)},\dots,\rho_m^{(e)},\gamma^{(e)}\mathbf{v}\right) - W^{L,\rho}\left(\rho_1^{(e)},\dots,\rho_m^{(e)},\gamma^{(e)}\mathbf{v}\right) \\ & + W^{L,\rho}\left(\rho_1^{(e)},\dots,\rho_m^{(e)},\mathbf{v}\right), \end{aligned} \tag{43}$$

where $\gamma^{(e)} \in [0,1]$ is an interpolation factor, and $W^{L,\rho}$ is the stored-energy function for isotropic linear elastic materials, which is given by

$$W^{L,\rho}\left(\rho_1^{(e)},\dots,\rho_m^{(e)},\mathbf{v}\right) = \mu_{\rho}(\rho_1^{(e)},\dots,\rho_m^{(e)})\boldsymbol{\varepsilon}(\mathbf{v}) : \boldsymbol{\varepsilon}(\mathbf{v}) + \frac{3\kappa_{\rho}(\rho_1^{(e)},\dots,\rho_m^{(e)}) - 2\mu_{\rho}(\rho_1^{(e)},\dots,\rho_m^{(e)})}{6}\left(\mathrm{tr}\boldsymbol{\varepsilon}(\mathbf{v})\right)^2, \tag{44}$$

where $\boldsymbol{\varepsilon}$ is the linearized strain tensor. In the above expression, μ_{ρ} and λ_{ρ} are the bulk and shear moduli interpolated from m candidate materials,

$$\mu_{\rho}(\rho_1^{(e)},\dots,\rho_m^{(e)}) = \sum_{i=1}^{m} w_i(\rho_1^{(e)},\dots,\rho_m^{(e)})\mu_i \quad \text{and} \quad \kappa_{\rho}(\rho_1^{(e)},\dots,\rho_m^{(e)}) = \sum_{i=1}^{m} w_i(\rho_1^{(e)},\dots,\rho_m^{(e)})\kappa_i, \tag{45}$$

where μ_i and κ_i are respectively the shear and bulk moduli for material i.

In the energy interpolation form (43), the interpolation factor $\gamma^{(e)}$ is defined using a smooth Heaviside function as

$$\gamma^{(e)}(\rho_1^{(e)},\dots,\rho_m^{(e)}) = \frac{\tanh(\beta_1\rho_0) + \tanh\left[\beta_1\left((\sum_{i=1}^{m}\overline{\rho}_i^{(e)})^p - \rho_0\right)\right]}{\tanh(\beta_1\rho_0) + \tanh\left[\beta_1(1-\rho_0)\right]}, \tag{46}$$

where β_1 is a sufficiently large number (e.g., $\beta_1 = 500$) and ρ_0 is a threshold. By definition, $\gamma^{(e)}$ can effectively distinguish between solid and void elements. If $\left(\sum_{i=1}^{m}\overline{\rho}_i^{(e)}\right)^p < \rho_0$, $\gamma_e \to 0$ and, according to (43), the behavior of element (e) is described by an isotropic linear elastic material $W^{L,\rho}$. When $\left(\sum_{i=1}^{m}\overline{\rho}_i^{(e)}\right)^p > \rho_0$, $\gamma_e \to 1$ and, according to (43), the behavior of element (e) is described by the true stored energy function W^{ρ}.

To simplify the expression, we realize that, for all $\gamma \in [0,1]$, $W^{L,\rho}\left(\rho_1^{(e)},\dots,\rho_m^{(e)},\mathbf{v}\right) - W^{L,\rho}\left(\rho_1^{(e)},\dots,\rho_m^{(e)},\gamma\mathbf{v}\right) = (1-\gamma^2)W^{L,\rho}\left(\rho_1^{(e)},\dots,\rho_m^{(e)},\mathbf{v}\right)$. We then obtain the simplified form of $W^{\rho,\gamma}$ as

$$\begin{aligned} & W^{\rho,\gamma}\left(\rho_1^{(e)},\dots,\rho_m^{(e)},\gamma^{(e)},\mathbf{v}\right) \\ & = W^{\rho}\left(\rho_1^{(e)},\dots,\rho_m^{(e)},\gamma^{(e)}\mathbf{v}\right) + \left(1-(\gamma^{(e)})^2\right)W^{L,\rho}\left(\rho_1^{(e)},\dots,\rho_m^{(e)},\mathbf{v}\right) \\ & = \sum_{i=1}^{m}\left[w_i(\rho_1^{(e)},\dots,\rho_m^{(e)})W_i\left(\mathbf{C}(\gamma^{(e)}\mathbf{v})\right)\right] + \left(1-(\gamma^{(e)})^2\right)W^{L,\rho}\left(\rho_1^{(e)},\dots,\rho_m^{(e)},\mathbf{v}\right). \end{aligned} \tag{47}$$

5.3. VEM approximation of the potential energy functional: material and energy interpolation schemes

Having introduced the material interpolation and the energy interpolation schemes to account for multiple hyperelastic materials under large deformations, the next step is to introduce the VEM approximation of the potential energy functional of the discretized system.

For a given discretization Ω_h and a set of design variables $\boldsymbol{\rho}_1, \ldots, \boldsymbol{\rho}_m$, we first assume exact integration within each element and write down the potential energy function Π_h of the discrete system as

$$\begin{aligned}\Pi_h(\boldsymbol{\rho}_1, \ldots, \boldsymbol{\rho}_m, \boldsymbol{\gamma}, \mathbf{v}_h) &= \sum_{E^{(e)} \in \Omega_h} \int_{E^{(e)}} W^{\rho,\gamma}\left(\rho_1^{(e)}, \ldots, \rho_m^{(e)}, \gamma^{(e)}, \mathbf{v}_h\right) \mathrm{d}\mathbf{X} - \int_{\Gamma_h^{\mathbf{t}}} \mathbf{t} \cdot \mathbf{v}_h \mathrm{d}S \\ &= \sum_{E^{(e)} \in \Omega_h} \Bigg[\sum_{i=1}^{m} w_i(\rho_1, \ldots, \rho_m) \int_{E^{(e)}} W_i\left(\mathbf{C}(\gamma^{(e)}\mathbf{v}_h)\right) \mathrm{d}\mathbf{X} \\ &\quad + \left(1 - (\gamma^{(e)})^2\right) \int_{E^{(e)}} W^{L,\rho}\left(\rho_1^{(e)}, \ldots, \rho_m^{(e)}, \mathbf{v}_h\right) \mathrm{d}\mathbf{X} \Bigg] - \int_{\Gamma_h^{\mathbf{t}}} \mathbf{t} \cdot \mathbf{v}_h \mathrm{d}S,\end{aligned} \tag{48}$$

where $\boldsymbol{\gamma}$ is a vector collecting $\gamma^{(e)}$ from all elements in the discretization.

In order to construct VEM approximations to the above potential energy functional, a crucial step is to approximate the following integrals over each element,

$$\int_{E^{(e)}} W_i\left(\mathbf{C}(\gamma^{(e)}\mathbf{v}_h)\right) \mathrm{d}\mathbf{X} \qquad \text{and} \qquad \int_{E^{(e)}} W^{L,\rho}\left(\rho_1^{(e)}, \ldots, \rho_m^{(e)}, \mathbf{v}_h\right) \mathrm{d}\mathbf{X}. \tag{49}$$

Following the concept of "consistency" and "stability" decomposition, we introduce the following VEM approximation of the first integral in (49) as

$$\begin{aligned}\int_{E^{(e)}} W_i\left(\mathbf{C}(\gamma^{(e)}\mathbf{v}_h)\right) \mathrm{d}\mathbf{X} &\approx |E^{(e)}| W_i\left(\mathbf{C}(\gamma^{(e)}\boldsymbol{\Pi}^{\nabla}_{E^{(e)}}\mathbf{v}_h)\right) \\ &\quad + \frac{\left(\gamma^{(e)}\right)^2}{2} \alpha_{E^{(e)},i}(\gamma^{(e)}\boldsymbol{\Pi}^{\nabla}_{E^{(e)}}\mathbf{v}_h) S_{h,E^{(e)}}\left(\mathbf{v}_h - \boldsymbol{\Pi}^{\nabla}_{E^{(e)}}\mathbf{v}_h, \mathbf{v}_h - \boldsymbol{\Pi}^{\nabla}_{E^{(e)}}\mathbf{v}_h\right) \doteq U_i^{(e)}\left(\gamma^{(e)}, \mathbf{v}_h\right),\end{aligned} \tag{50}$$

where we recall that the stability parameter for the ith material $\alpha_{E^{(e)},i}$ is evaluated as:

$$\alpha_{E^{(e)},i}(\gamma^{(e)}\boldsymbol{\Pi}^{\nabla}_{E^{(e)}}\mathbf{v}_h) = \frac{1}{4}\mathrm{tr}\left[\frac{\partial^2 W_i}{\partial \mathbf{F} \partial \mathbf{F}}\left(\mathbf{C}(\gamma^{(e)}\boldsymbol{\Pi}^{\nabla}_{E^{(e)}}\mathbf{v}_h)\right)\right], \tag{51}$$

according to expressions (31) or (33). To simplify expressions, we use $U_i^{(e)}$ to denote the VEM approximation of the strain energy of element (e) associated with the ith material in the remainder of this section.

Similarly, the second integral in (49) is approximated as

$$\begin{aligned}\int_{E^{(e)}} W^{L,\rho}\left(\rho_1^{(e)}, \ldots, \rho_m^{(e)}, \mathbf{v}_h\right) \mathrm{d}\mathbf{X} &\approx \Bigg[|E^{(e)}| W^{L,\rho}\left(\rho_1^{(e)}, \ldots, \rho_m^{(e)}, \boldsymbol{\Pi}^{\nabla}_{E^{(e)}}(\mathbf{v}_h)\right) \\ &\quad + \frac{\alpha_{E^{(e)},L}(\rho_1^{(e)}, \ldots, \rho_m^{(e)})}{2} S_{h,E^{(e)}}\left(\mathbf{v}_h - \boldsymbol{\Pi}^{\nabla}_{E^{(e)}}\mathbf{v}_h, \mathbf{v}_h - \boldsymbol{\Pi}^{\nabla}_{E^{(e)}}\mathbf{v}_h\right) \Bigg] \\ &\doteq U_L^{(e)}\left(\rho_1^{(e)}, \ldots, \rho_m^{(e)}, \mathbf{v}_h\right),\end{aligned} \tag{52}$$

where the stability parameter $\alpha_{E^{(e)},L}$ is computed as the normalized trace of the elasticity tensor for isotropic linear elastic materials as

$$\alpha_{E^{(e)},L}(\rho_1^{(e)}, \ldots, \rho_m^{(e)}) = \frac{1}{2}\kappa_\rho(\rho_1^{(e)}, \ldots, \rho_m^{(e)}) + \frac{7}{6}\mu_\rho(\rho_1^{(e)}, \ldots, \rho_m^{(e)}). \tag{53}$$

To simplify expressions, we denote the above VEM approximation (52) as $U_L^{(e)}$ in the remainder of this section.

With the VEM approximations of the two integrals in (49), the VEM approximation of the potential energy functional Π_h, which is denoted Π_h^{VEM}, is given by

$$\Pi_h^{VEM}\Big(\boldsymbol{\rho}_1,\ldots,\boldsymbol{\rho}_m,\boldsymbol{\gamma},\mathbf{v}_h\Big) = \sum_{E^{(e)}\in\Omega_h}\left\{\sum_{i=1}^{m}\Big[w_i(\rho_1^{(e)},\ldots,\rho_m^{(e)})U_i^{(e)}\Big(\gamma^{(e)},\mathbf{v}_h\Big)\Big] + \Big(1-(\gamma^{(e)})^2\Big)U_L^{(e)}\Big(\rho_1^{(e)},\ldots,\rho_m^{(e)},\mathbf{v}_h\Big)\right\} - \langle\mathbf{t},\mathbf{v}_h\rangle_h, \tag{54}$$

where $\langle\mathbf{t},\mathbf{v}\rangle_h$ is the VEM approximation of the external energy [50].

We remark that, instead of using the above VEM approximation of the potential energy, one can also adopt a Finite Element (FE) approximation as described in the Appendix. By comparing the expressions for the potential energy using a lower-order VEM (54) and a lower-order FEM (89), we notice that to compute the potential energy of the multi-material system, the VEM approximation requires a total of $m+1$ evaluations (since $\nabla\boldsymbol{\Pi}_E^{\nabla}\mathbf{v}_h$ is constant for each element domain E), whereas the FEM approximation needs a total of $(m+1)\times N_E^Q$ evaluations, with m the total number of candidate materials and N_E^Q the total number of numerical integration points in element domain E. Note that the potential energy and its linearizations need to be evaluated multiple times at each optimization step; thus, the fewer functional evaluations needed for the VEM (for grids other than triangular/tetrahedral) can lead to considerable computational cost savings. In the meantime, we also note that the above discussions assume FEM approximation with full integration. One can also apply FEM approximation with reduced integration [79] to achieve a similar computational cost as the VEM approximation.

5.4. VEM-based multi-material topology optimization formulation to maximize equilibrating potential energy

The first topology optimization formulation considered in this work aims to maximize the potential energy of the structure at its equilibrium state, which corresponds to maximizing the overall stiffness of the structure [70,73,80–82]. The specific form of the objective function is given as:

$$J\left(\boldsymbol{\rho}_1,\ldots,\boldsymbol{\rho}_m\right) = -\Pi_h^{VEM}\Big(\boldsymbol{\rho}_1,\ldots,\boldsymbol{\rho}_m,\boldsymbol{\gamma},\mathbf{u}_h\left(\boldsymbol{\rho}_1,\ldots,\boldsymbol{\rho}_m\right)\Big), \tag{55}$$

where Π_h^{VEM} is the VEM approximation of the potential energy introduced in (54).

In order to compute the sensitivity of the objective function, we need to compute the sensitivity of the potential energy with respect to the filtered design variable $\overline{\rho}_i^{(e)}$ as

$$\begin{aligned}\frac{\partial\Pi_h^{VEM}}{\partial\overline{\rho}_i^{(e)}} &= \frac{\partial\Pi_h^{VEM}}{\partial w_j}\frac{\partial w_j}{\partial\overline{\rho}_i^{(e)}} + \frac{\partial\Pi_h^{VEM}}{\partial\gamma^{(e)}}\frac{\partial\gamma^{(e)}}{\partial\overline{\rho}_i^{(e)}} + \frac{\partial\Pi_h^{VEM}}{\partial\mathbf{u}_h}\frac{\partial\mathbf{u}_h}{\partial\overline{\rho}_i^{(e)}}\\ &= \sum_{j=1}^{m}\Big[U_j^{(e)} + \Big(1-(\gamma^{(e)})^2\Big)\frac{\partial U_L^{(e)}}{\partial w_j}\Big]\frac{\partial w_j}{\partial\overline{\rho}_i^{(e)}} + \Big[\sum_{k=1}^{m}w_k\frac{\partial U_k^{(e)}}{\partial\gamma^{(e)}} - 2\gamma^{(e)}U_L^{(e)}\Big]\frac{\partial\gamma^{(e)}}{\partial\overline{\rho}_i^{(e)}}.\end{aligned} \tag{56}$$

In the above relation, the third term in the intermediate step vanishes because $\mathbf{u}_h$ satisfies the equilibrium condition.

According to the expressions of $U_i^{(e)}$ and $U_L^{(e)}$, we have the following relations:

$$\begin{aligned}\frac{\partial U_L^{(e)}}{\partial w_j} &= |E^{(e)}|\Big[\mu_j\boldsymbol{\varepsilon}(\boldsymbol{\Pi}_E^{\nabla}\mathbf{v}_h):\boldsymbol{\varepsilon}(\boldsymbol{\Pi}_E^{\nabla}\mathbf{v}_h) + \frac{3\kappa_j-2\mu_j}{6}\Big(\mathrm{tr}\boldsymbol{\varepsilon}(\boldsymbol{\Pi}_E^{\nabla}\mathbf{v}_h)\Big)^2\Big]\\ &\quad+\Big[\frac{1}{4}\kappa_j+\frac{7}{12}\mu_j\Big]S_{h,E^{(e)}}(\mathbf{v}_h-\boldsymbol{\Pi}_{E^{(e)}}^{\nabla}\mathbf{v}_h,\mathbf{v}_h-\boldsymbol{\Pi}_{E^{(e)}}^{\nabla}\mathbf{v}_h);\end{aligned} \tag{57}$$

$$\begin{aligned}\frac{\partial U_j^{(e)}}{\partial\gamma^{(e)}} &= \Big[|E^{(e)}|\frac{\partial W_j}{\partial\mathbf{F}}\Big(\mathbf{C}(\gamma^{(e)}\boldsymbol{\Pi}_{E^{(e)}}^{\nabla}\mathbf{v}_h)\Big)\\ &\quad+\frac{(\gamma^{(e)})^2}{2}S_{h,E^{(e)}}(\mathbf{v}_h-\boldsymbol{\Pi}_{E^{(e)}}^{\nabla}\mathbf{v}_h,\mathbf{v}_h-\boldsymbol{\Pi}_{E^{(e)}}^{\nabla}\mathbf{v}_h)\frac{\partial\alpha_{E^{(e)},j}}{\partial\mathbf{F}}(\gamma^{(e)}\boldsymbol{\Pi}_{E^{(e)}}^{\nabla}\mathbf{v}_h)\Big]:\nabla\Big(\boldsymbol{\Pi}_E^{\nabla}\mathbf{v}_h\Big)\\ &\quad+\gamma^{(e)}\alpha_{E^{(e)},j}(\gamma^{(e)}\boldsymbol{\Pi}_{E^{(e)}}^{\nabla}\mathbf{v}_h)S_{h,E^{(e)}}(\mathbf{v}_h-\boldsymbol{\Pi}_{E^{(e)}}^{\nabla}\mathbf{v}_h,\mathbf{v}_h-\boldsymbol{\Pi}_{E^{(e)}}^{\nabla}\mathbf{v}_h);\end{aligned} \tag{58}$$

and

$$\frac{\partial\gamma^{(e)}}{\partial\overline{\rho}_i^{(e)}} = p\Big(\sum_{j=1}^{m}\overline{\rho}_i^{(e)}\Big)^{p-1}\left\{\frac{\beta_1\Big[\tanh\Big(\beta_1\Big(\Big(\sum_{j=1}^{m}\overline{\rho}_j^{(e)}\Big)^p-\rho_0\Big)\Big)^2-1\Big]}{\tanh\Big(\beta_1(\rho_0-1)\Big)-\tanh\Big(\beta_1\rho_0\Big)}\right\}; \tag{59}$$

where the derivative of $\alpha_{E^{(e)},j}$ with respect to $\mathbf{F}$ can be obtained using the explicit expressions for α_E (see (31) and (33)) following the same procedure as in Section 3 for computing the derivatives of the stored-energy functions. In addition, the expression for $\partial w_j/\partial \overline{\rho}_i^{(e)}$ depends on the material interpolation scheme considered. Using the DMO-type material interpolation scheme (see Section 5.1), we have

$$\frac{\partial w_j}{\partial \overline{\rho}_i^{(e)}} = \begin{cases} p\left[\left(\overline{\rho}_i^{(e)}\right)^{p-1}\prod_{l=1,l\neq i}^{m}\left(1-(\overline{\rho}_l^{(e)})^p\right)\right] & \text{if } i=j, \\ -p\left[\left(\overline{\rho}_i^{(e)}\right)^{p-1}\left(\overline{\rho}_j^{(e)}\right)^{p}\prod_{l=1,l\neq i,l\neq j}^{m}\left(1-(\overline{\rho}_l^{(e)})^p\right)\right] & \text{if } i\neq j. \end{cases} \tag{60}$$

Once the sensitivity of the potential energy with respect to the filtered design variable $\overline{\rho}_i^{(e)}$ is computed, the sensitivity of the objective function J is given by

$$\frac{\partial J}{\partial \rho_i^{(e)}} = -\sum_k (\mathbf{P}_i)_{k,e}\frac{\partial \Pi_h^{VEM}}{\partial \overline{\rho}_i^{(k)}}, \tag{61}$$

where we recall that $(\mathbf{P}_i)_{k,e}$ is the (k,e)th component of the filter matrix $\mathbf{P}_i$ associated with the ith candidate material.

5.5. VEM-based multi-material topology optimization formulation for compliant mechanism design

To demonstrate the generality of the proposed VEM-based multi-material topology optimization formulation, we also consider compliant mechanism designs [13,83–85]. The objective function of such problems has the form

$$J\left(\boldsymbol{\rho}_1,\ldots,\boldsymbol{\rho}_m\right) = \mathbf{L}^T\mathbf{U}(\boldsymbol{\rho}_1,\ldots,\boldsymbol{\rho}_m), \tag{62}$$

where $\mathbf{U}$ represents the nodal displacement vector of $\mathbf{u}_h$, and $\mathbf{L}$ is a constant vector whose components are 1 at output DOFs and 0 everywhere else.

The sensitivity of J with respect to the filtered design variable $\overline{\rho}_i^{(e)}$ can be computed through the chain rule and adjoint method [64] as follows:

$$\frac{\partial J}{\partial \overline{\rho}_i^{(e)}} = \boldsymbol{\lambda}^T\left[\frac{\partial \mathbf{F}_{\text{int}}}{\partial w_j}\frac{\partial w_j}{\partial \overline{\rho}_i^{(e)}} + \frac{\partial \mathbf{F}_{\text{int}}}{\partial \gamma^{(e)}}\frac{\partial \gamma^{(e)}}{\partial \overline{\rho}_i^{(e)}}\right], \tag{63}$$

where $\mathbf{F}_{\text{int}} \doteq \partial \Pi_h^{VEM}/\partial \mathbf{U}$ stands for the internal force vector of the VEM approximation and $\boldsymbol{\lambda}$ is the adjoint vector obtained by solving the following linear system of equations:

$$\boldsymbol{\lambda} = -\mathbf{K}_t^{-1}(\boldsymbol{\rho}_1,\ldots,\boldsymbol{\rho}_m,\boldsymbol{\gamma},\mathbf{u}_h)\mathbf{L}, \tag{64}$$

where $\mathbf{K}_t \doteq \partial^2 \Pi_h^{VEM}/\partial \mathbf{U}\partial \mathbf{U}$ is the tangent stiffness matrix evaluated at the converged solution $\mathbf{u}_h$. Expressions for the derivatives in (63) can be computed in the similar fashion as those in the preceding subsection.

Once the sensitivity of the objective function with respect to the filtered design variable is obtained, that of the objective function with respect to the design variable is given by

$$\frac{\partial J}{\partial \rho_i^{(e)}} = \sum_k (\mathbf{P}_i)_{k,e}\frac{\partial J}{\partial \overline{\rho}_i^{(k)}}. \tag{65}$$

6. A modified ZPR design update scheme

The ZPR design update scheme, proposed in [7] for multi-material topology optimization, is capable of updating an arbitrary number of volume constraints while preserving the efficiency and robustness of the popular Optimality Criteria (OC) method, which is limited to a single volume constraint. In particular, the ZPR design update scheme separates the updates of the design variables associated with each volume constraint and performs the updates independently. The original ZPR update scheme only allows for the optimization problems whose objectives always have negative sensitivities. However, for the multi-material topology optimization considered in this work, positive sensitivities can occur. Thus, an improved version of the ZPR design update scheme is introduced to allow for positive sensitivities, while preserving all the features of the original ZPR update scheme.

Inspired by [86], our idea is to introduce the following modified optimization problem of (34)

$$\begin{aligned}
&\min_{\boldsymbol{\rho}_1,\ldots,\boldsymbol{\rho}_m} \quad \left[J\left(\boldsymbol{\rho}_1,\ldots,\boldsymbol{\rho}_m\right) - \sum_{j=1} \mu^j \sum_{i\in\mathcal{G}^j} \overline{\mathbf{V}}_i^T \boldsymbol{\rho}_i \right] \\
&\text{s.t.} \quad g^j\left(\boldsymbol{\rho}_1,\ldots,\boldsymbol{\rho}_m\right) = \sum_{i\in\mathcal{G}^j} \overline{\mathbf{V}}_i^T \boldsymbol{\rho}_i - V^j_{\max} \leq 0, \quad j=1,\ldots,nc, \\
&\qquad \rho_{\min} \leq \rho_i^{(e)} \leq 1, \; i=1,\ldots,m, \;\text{ and } e=1,\ldots,M, \\
&\text{with } \mathbf{u}_h\left(\boldsymbol{\rho}_1,\ldots,\boldsymbol{\rho}_m\right) = \arg\min_{\mathbf{v}_h} \Pi_h^{VEM}\left(\boldsymbol{\rho}_1,\ldots,\boldsymbol{\rho}_m,\mathbf{v}_h\right),
\end{aligned} \tag{66}$$

where μ^j, $j=1,\ldots,nc$ are positive constants. Notice that in the modified problem, we augment the objective with a linear term on the design variables. In the following discussion, we denote the modified objective as $\widehat{J}$.

It can be shown that the original and the modified optimization problems are equivalent in the sense that they possess the same local minima. In fact, the Karush–Kuhn–Tucker (KKT) conditions of the original optimization problem (34) take the following form:

$$\frac{\partial J}{\partial \rho_i^{(e)}} + \phi^{\mathcal{M}_i} \overline{V}_i^{(e)} - \underline{\phi}_i^{(e)} + \overline{\phi}_i^{(e)} = 0, \tag{67}$$

$$\sum_{i\in\mathcal{G}^j} \overline{\mathbf{V}}^T \boldsymbol{\rho}_i - V^j_{\max} = 0, \quad j=1...,nc, \tag{68}$$

$$\begin{cases} \underline{\phi}_i^{(e)} > 0 & \text{if } \rho_i^{(e)} = \rho_{\min} \\ \underline{\phi}_i^{(e)} = 0 & \text{if } \rho_i^{(e)} > \rho_{\min} \end{cases} \text{ and } \begin{cases} \overline{\phi}_i^{(e)} > 0 & \text{if } \rho_i^{(e)} = 1 \\ \overline{\phi}_i^{(e)} = 0 & \text{if } \rho_i^{(e)} < 1, \end{cases} \tag{69}$$

where $\mathcal{M}_i$ denotes the volume constraint index associated with the ith material (e.g, if material 3 is assigned to the 1st volume constraint, then $\mathcal{M}_3 = 1$), and thus $\phi^{\mathcal{M}_i}$ is the Lagrange multiplier associated with material i. On the other hand, the KKT conditions for the modified problem are identical to the original problem except for the first condition:

$$\frac{\partial J}{\partial \rho_i^{(e)}} - \mu^{\mathcal{M}_i} \overline{V}_i^{(e)} + (\widehat{\phi}^{\mathcal{M}_i}) \overline{V}_i^{(e)} - \underline{\phi}_i^{(e)} + \overline{\phi}_i^{(e)} = 0, \tag{70}$$

where we recall that $\mu^{\mathcal{M}_i}$ is a positive constant. By comparing the KKT conditions of the original and modified optimization problems, we conclude that both problems always have the same local minima. Moreover, if the optimal Lagrange multiplier of volume constraint j for a given local minimum is ϕ^j in the original problem, then the corresponding Lagrange multiplier for the volume constraint in the modified problem is $\hat{\phi}^j = \phi^j + \mu^j$.

Having introduced the modified optimization problem, we then perform sequential approximation on the modified objective $\widehat{J}$. As we will demonstrate later, by properly choosing the constants μ^j, the convexity of the sequential approximation can be ensured. Once the solution converges to a KKT point of the modified problem, by the equivalence of the KKT conditions between the original and modified problems, we ensure that this converged solution is a KKT point of the original problem as well.

Following the original derivation of ZPR design update scheme, at each optimization step k, we introduce an approximation of the objective function $\widehat{J}$ at the optimization step k over $\mathbf{y}_i(\boldsymbol{\rho}_i)$ ($y_i^{(e)}(\rho_i^{(e)}) \doteq (\rho_i^{(e)})^{-\alpha}$, $i=1,\ldots,m$ and $e=1,\ldots,M$) as follows,

$$\begin{aligned}
\widehat{J}\left(\boldsymbol{\rho}_1,\ldots,\boldsymbol{\rho}_m\right) &\approx \widehat{J}^k\left(\boldsymbol{\rho}_1,\ldots,\boldsymbol{\rho}_m\right) = \widehat{J}\left(\boldsymbol{\rho}_1^k,\ldots,\boldsymbol{\rho}_m^k\right) + \sum_{i=1}^m \left[\frac{\partial \widehat{J}}{\partial \mathbf{y}_i}(\boldsymbol{\rho}_1^k,\ldots,\boldsymbol{\rho}_m^k)\right]^T \left[\mathbf{y}_i(\boldsymbol{\rho}_i) - \mathbf{y}_i(\boldsymbol{\rho}_i^k)\right] \\
&= \widehat{J}\left(\boldsymbol{\rho}_1^k,\ldots,\boldsymbol{\rho}_m^k\right) + \sum_{i=1}^m \left[\widehat{\mathbf{b}}_i(\boldsymbol{\rho}_1^k,\ldots,\boldsymbol{\rho}_m^k)\right]^T \left[\mathbf{y}_i(\boldsymbol{\rho}_i) - \mathbf{y}_i(\boldsymbol{\rho}_i^k)\right],
\end{aligned} \tag{71}$$

where α is an arbitrary, strictly positive number, $\boldsymbol{\rho}_i^k$ and $\mathbf{y}_i(\boldsymbol{\rho}_i^k)$ are the vectors of design and intervening variables at the kth optimization step for material i. Additionally, $\widehat{\mathbf{b}}_i(\boldsymbol{\rho}_1^k,\ldots,\boldsymbol{\rho}_m^k)$ is a constant vector associated with material

i, whose eth component is given as follows:

$$\widehat{b}_i^{(e)}(\boldsymbol{\rho}_1^k,\ldots,\boldsymbol{\rho}_m^k) = \frac{\partial \widehat{J}}{\partial y_i^{(e)}}(\boldsymbol{\rho}_1^k,\ldots,\boldsymbol{\rho}_m^k) = -\frac{(\rho_i^{(e),k})^{1+\alpha}}{\alpha}\frac{\partial \widehat{J}}{\partial \rho_i^{(e)}}(\boldsymbol{\rho}_1^k,\ldots,\boldsymbol{\rho}_m^k)$$
$$= -\frac{(\rho_i^{(e),k})^{1+\alpha}}{\alpha}\left[\frac{\partial J}{\partial \rho_i^{(e)}}(\boldsymbol{\rho}_1^k,\ldots,\boldsymbol{\rho}_m^k) - \mu^{\mathcal{M}_i}\overline{V}_i^{(e)}\right]. \tag{72}$$

To ensure convexity of the subproblem, the constant $\mu^{\mathcal{M}_i}$ needs to satisfy

$$-\frac{(\rho_i^{(e),k})^{1+\alpha}}{\alpha}\left[\frac{\partial J}{\partial \rho_i^{(e)}}(\boldsymbol{\rho}_1^k,\ldots,\boldsymbol{\rho}_m^k) - \mu^{\mathcal{M}_i}\overline{V}_i^{(e)}\right] > 0, \tag{73}$$

for all the components of material i and all the materials.

Using the approximated objective function $\widehat{J}^k$, a subproblem is formulated at step k as

$$\begin{aligned}
\min_{\boldsymbol{\rho}_1,\ldots,\boldsymbol{\rho}_m}\quad & \widehat{J}^k\left(\boldsymbol{\rho}_1,\ldots,\boldsymbol{\rho}_m\right) = \min_{\boldsymbol{\rho}_1,\ldots,\boldsymbol{\rho}_m}\left\{\sum_{i=1}^{m}\left[\widehat{\mathbf{b}}_i(\boldsymbol{\rho}_1^k,\ldots,\boldsymbol{\rho}_m^k)\right]^T\left[\mathbf{y}_i(\boldsymbol{\rho}_i)-\mathbf{y}_i(\boldsymbol{\rho}_i^k)\right]\right\}\\
\text{s.t.}\quad & \sum_{i\in\mathcal{G}^j}\overline{\mathbf{V}}_i^{\mathrm{T}}\boldsymbol{\rho}_i - V_{\max}^j \le 0,\ \ j=1,\ldots,nc,\\
& \rho_{i,\mathrm{L}}^{(e),k} \le \rho_i^{(e)} \le \rho_{i,\mathrm{U}}^{(e),k},\ i=1,\ldots,m,\ \text{and } e=1,\ldots,M,\\
& \text{with } y_i^{(e)}(x_i^{(e)}) = (\rho_i^{(e)})^{-\alpha},\ i=1,\ldots,m,\ \text{and } e=1,\ldots,M,
\end{aligned} \tag{74}$$

where $\rho_{i,\mathrm{L}}^{(e),k} = \max(\rho_{\min}, \rho_i^{(e),k} - move)$ and $\rho_{i,\mathrm{U}}^{(e),k} = \min(1, \rho_i^{(e),k} + move)$ are the upper and lower bounds of the design variables, which are determined through the prescribed move limit, $move$. In the above subproblem, the constant term in $\widehat{J}^k$ has been omitted.

By introducing a set of Lagrange multipliers $\widehat{\phi}^{j,k}$, $j=1,\ldots,nc$, the Lagrangian of the subproblem in Eq. (74) takes the following form:

$$\mathcal{L}\left(\boldsymbol{\rho}_1,\ldots,\boldsymbol{\rho}_m,\widehat{\phi}^{1,k},\ldots,\widehat{\phi}^{nc,k}\right) = \sum_{i=1}^{m}\left[\widehat{\mathbf{b}}_i(\boldsymbol{\rho}_1^k,\ldots,\boldsymbol{\rho}_m^k)\right]^T\mathbf{y}_i(\boldsymbol{\rho}_i) + \sum_{j=1}^{nc}\widehat{\phi}^{j,k}\left(\sum_{i\in\mathcal{G}^j}\overline{\mathbf{V}}_i^{\mathrm{T}}\boldsymbol{\rho}_i - V_{\max}^j\right). \tag{75}$$

Notice that the above Lagrangian is a separable function for each volume constraint, namely,

$$\begin{aligned}
&\mathcal{L}\left(\boldsymbol{\rho}_1,\ldots,\boldsymbol{\rho}_m,\widehat{\phi}^{1,k},\ldots,\widehat{\phi}^{nc,k}\right) = \sum_{j=1}^{nc}\mathcal{L}^j\left(\boldsymbol{\rho}_1,\ldots,\boldsymbol{\rho}_m,\widehat{\phi}^{j,k}\right)\\
&= \sum_{j=1}^{nc}\left\{\sum_{i\in\mathcal{G}^j}\left[\left[\widehat{\mathbf{b}}_i(\boldsymbol{\rho}_1^k,\ldots,\boldsymbol{\rho}_m^k)\right]^T\mathbf{y}_i(\boldsymbol{\rho}_i) + \widehat{\phi}^{j,k}\overline{\mathbf{V}}_i^{\mathrm{T}}\boldsymbol{\rho}_i\right] - \widehat{\phi}^{j,k}V_{\max}^j\right\}.
\end{aligned} \tag{76}$$

The KKT conditions of the subproblem (74) require that

$$\frac{\mathcal{L}}{\partial \rho_i^{(e)}} = \frac{\mathcal{L}^j}{\partial \rho_i^{(e)}} = -\alpha\widehat{b}_i^{(e)}(\boldsymbol{\rho}_1^k,\ldots,\boldsymbol{\rho}_m^k)\left(\rho_i^{(e)}\right)^{(-\alpha-1)} + \widehat{\phi}^{j,k}\overline{V}_i^{(e)} = 0, \quad \forall i \in \mathcal{G}^j, \tag{77}$$

and

$$\frac{\mathcal{L}}{\partial \widehat{\phi}^{j,k}} = \sum_{i\in\mathcal{G}^j}\overline{\mathbf{V}}_i^{\mathrm{T}}\boldsymbol{\rho}_i - V_{\max}^j = 0, \quad j=1,\ldots,nc. \tag{78}$$

From (77), we can write the solution $\rho_i^{(e)*}$ as

$$\rho_i^{(e)*} = Q_i^{(e),k}\left(\widehat{\phi}^{j,k}\right) = \left[\frac{\alpha\widehat{b}_i^{(e)}(\boldsymbol{\rho}_1^k,\ldots,\boldsymbol{\rho}_m^k)}{\widehat{\phi}^{j,k}\,\overline{V}_i^{(e)}}\right]^{\frac{1}{1+\alpha}}, \quad \forall i \in \mathcal{G}^j. \tag{79}$$

By further incorporating the lower and upper bounds, $\boldsymbol{\rho}_{i,\mathrm{L}}^{k}$, and $\boldsymbol{\rho}_{i,\mathrm{U}}^{k}$, of the design variables, the expression for $\rho_i^{(e)*}$ is modified as

$$\rho_i^{(e)*} = Q_i^{(e),k}\left(\widehat{\phi}^{j,k}\right) = \begin{cases} \rho_{i,\mathrm{L}}^{(e),k} & \text{if } \left[\dfrac{\alpha \widehat{b}_i^{(e)}(\boldsymbol{\rho}_1^k,\ldots,\boldsymbol{\rho}_m^k)}{\widehat{\phi}^j\,\overline{V}_i^{(e)}}\right]^{\frac{1}{1+\alpha}} < \rho_{i,\mathrm{L}}^{(e),k} \\ \left[\dfrac{\alpha \widehat{b}_i^{(e)}(\boldsymbol{\rho}_1^k,\ldots,\boldsymbol{\rho}_m^k)}{\widehat{\phi}_{j,k}\,\overline{V}_i^{(e)}}\right]^{\frac{1}{1+\alpha}} & \text{if } \rho_{i,\mathrm{L}}^{(e),k} \le \left[\dfrac{\alpha \widehat{b}_i^{(e)}(\boldsymbol{\rho}_1^k,\ldots,\boldsymbol{\rho}_m^k)}{\widehat{\phi}^{j,k}\,\overline{V}_i^{(e)}}\right]^{\frac{1}{1+\alpha}} \le \rho_{i,\mathrm{U}}^{(e),k}\,, \quad \forall i \in \mathcal{G}^j. \\ \rho_{i,\mathrm{U}}^{(e),k} & \text{if } \left[\dfrac{\alpha \widehat{b}_i^{(e)}(\boldsymbol{\rho}_1^k,\ldots,\boldsymbol{\rho}_m^k)}{\widehat{\phi}^{j,k}\,\overline{V}_i^{(e)}}\right]^{\frac{1}{1+\alpha}} > \rho_{i,\mathrm{U}}^{(e),k} \end{cases} \tag{80}$$

Plugging in the expressions for $\widehat{b}_i^{(e)}$ given by (72) and introducing the damping factor $\eta = 1/(1+\alpha)$, we can further simplify $\rho_i^{(e)*}$ as

$$Q_i^{(e),k}\left(\widehat{\phi}^{j,k}\right) = \begin{cases} \rho_{i,\mathrm{L}}^{(e),k} & \text{if } \left[\dfrac{\rho_i^{(e)k}}{\widehat{\phi}^{j,k}}\left(-\dfrac{\partial J/\partial \rho_i^{(e)}(\boldsymbol{\rho}_1^k,\ldots,\boldsymbol{\rho}_m^k)}{\overline{V}_i} + \mu^j\right)\right]^{\eta} < \rho_{i,\mathrm{L}}^{(e),k} \\ \left[\dfrac{\rho_i^{(e)k}}{\widehat{\phi}^{j,k}}\left(-\dfrac{\partial J/\partial \rho_i^{(e)}(\boldsymbol{\rho}_1^k,\ldots,\boldsymbol{\rho}_m^k)}{\overline{V}_i} + \mu^j\right)\right]^{\eta} & \text{if } \rho_{i,\mathrm{L}}^{(e),k} \le \left[\dfrac{\rho_i^{(e)k}}{\widehat{\phi}^{j,k}}\left(-\dfrac{\partial J/\partial \rho_i^{(e)}(\boldsymbol{\rho}_1^k,\ldots,\boldsymbol{\rho}_m^k)}{\overline{V}_i} + \mu^j\right)\right]^{\eta} \le \rho_{i,\mathrm{U}}^{(e),k}\,, \\ \rho_{i,\mathrm{U}}^{(e),k} & \text{if } \left[\dfrac{\rho_i^{(e)k}}{\widehat{\phi}^{j,k}}\left(-\dfrac{\partial J/\partial \rho_i^{(e)}(\boldsymbol{\rho}_1^k,\ldots,\boldsymbol{\rho}_m^k)}{\overline{V}_i} + \mu^j\right)\right]^{\eta} > \rho_{i,\mathrm{U}}^{(e),k} \end{cases}$$
$$\forall i \in \mathcal{G}^j. \tag{81}$$

According to (73), at optimization step k, if we choose the constants μ^j, $j = 1,\ldots,nc$, such that

$$\mu^j \ge \max\left(0, \frac{\partial J/\partial \rho_i^{(e)}(\boldsymbol{\rho}_1^k,\ldots,\boldsymbol{\rho}_m^k)}{\overline{V}_i}\right) \quad \forall e \text{ and } \forall i \in \mathcal{G}^j, \tag{82}$$

we can guarantee that the subproblem is convex and function $Q_i^{(e),k}\left(\widehat{\phi}^j\right)$ is a real-valued function for any $0 < \eta \le 1$.

Remark 6.1. The choice of constant μ^j can be flexible as long as it satisfies Eq. (82). For the topology optimization problem (34) considered in this work, we find that the performance of the modified ZPR is insensitive to different choices of μ^j. Thus, μ^j is chosen based on the following rule throughout this work:

$$\mu^j = \max\left(0, \max_{i\in\mathcal{G}^j}\left(\max_e\left(\frac{\partial J/\partial \rho_i^{(e)}(\boldsymbol{\rho}_1^k,\ldots,\boldsymbol{\rho}_m^k)}{\overline{V}_i}\right)\right)\right). \tag{83}$$

By plugging (80) back into Eq. (78), we have

$$\frac{\partial \mathcal{L}}{\partial \widehat{\phi}^{j,k}} = \sum_{i\in\mathcal{G}^j}\sum_{e=1}^{M} \overline{V}_i^{(e)} \rho_i^{(e)*}\left(\widehat{\phi}^{j,k}\right) - V_{\max}^j = 0, \quad j = 1,\ldots,nc, \tag{84}$$

where $\overline{V}_i^{(e)}$ stands for the eth component of $\overline{\mathbf{V}}_i$. Notice that the jth equation of the above system is an algebraic equation of $\widehat{\phi}^{j,k}$ only. Therefore, we have a decoupled system with respect to the volume constraints in which each optimal Lagrange multiplier ϕ can be solved for independently by their corresponding equations.

Finally, the update of the eth component of design variables $\boldsymbol{\rho}_i^{k+1}$ then take as the optimal solution in the subproblem (74) as:

$$\rho_i^{(e),k+1} = Q_i^{(e),k}\left(\widehat{\phi}_*^{j,k}\right), \quad \forall i \in \mathcal{G}^j. \tag{85}$$

We note that the update in (85) is decoupled in the sense that the updates of the design variables associated with each volume constraint only depends on the associated optimal Lagrange multiplier $\widehat{\phi}^{j*}$. This feature, together with the feature of decoupled solution of $\widehat{\phi}^{j*}$ in (84), enables us to update the associated design variables of each volume constraint in parallel throughout the entire optimization process — an attractive feature of the ZPR design update scheme to promote increased efficiency in large-scale multi-material topology optimization problems.

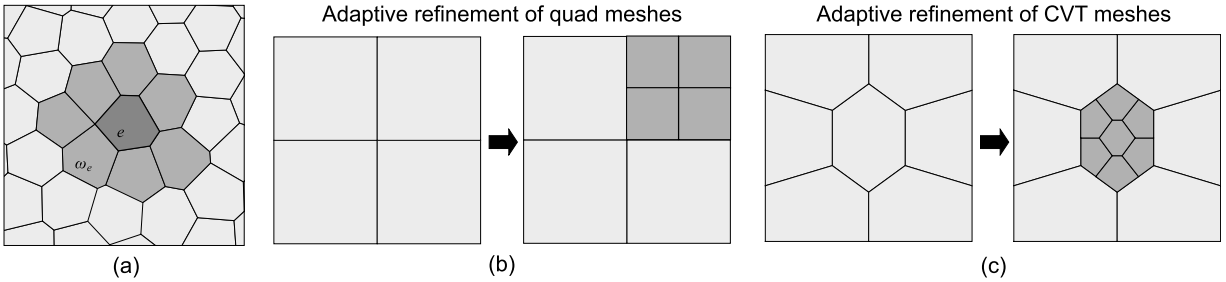

Fig. 1. Illustrations of (a) the patch of elements for element (e); (b) the refinement strategy for a quadrilateral mesh; and (c) the refinement strategy for a CVT mesh.

7. Adaptive mesh refinement and coarsening for the VEM-based multi-material topology optimization

Topology optimization considering multiple hyperelastic materials is a computationally intensive task because, at every optimization iteration, we need to solve a nonlinear system of equations to obtain the equilibrium displacement field. To overcome this challenge, we introduce an adaptive refinement and coarsening strategy for the proposed VEM-based multi-material topology optimization, such that we refine the regions where the material densities have high spatial variations and coarsen the regions where the material densities have low spatial variations. This idea fully exploits the advantages of VEM in handling arbitrary element shapes.

We remark that, in this work, the adaptive refinement and coarsening is only performed between optimization steps and the indicators for both adaptive refinement and coarsening are based on the density fields. Other indicators, such as those based on displacements and strains [87], could also be adopted.

7.1. Adaptive refinement

The adaptive refinement process is driven by an indicator defined in the following manner. We denote $\boldsymbol{\Theta}$ as the indicator vector whose eth component, $\Theta^{(e)}$, is the indicator for element (e). To define $\Theta^{(e)}$, we first introduce ω_e as the patch of elements which are connected to element (e), as illustrated in Fig. 1(a). Assuming ω_e contains N_{ω_e} elements, we then define the indicator $\Theta^{(e)}$ for element (e) as

$$\Theta^{(e)} = \max_{i\in\{1,\dots,m\}} \left\{ \frac{1}{N_{\omega_e}} \left[\sum_{E^{(k)}\in\omega_e} \left(\rho_i^{(k)} - \rho_i^{(e)} \right)^2 \right]^{\frac{1}{2}} \right\}. \tag{86}$$

At a given optimization step, once we compute the indicator $\boldsymbol{\Theta}$, we can mark the set of elements whose indicators are above $\theta \max(\boldsymbol{\Theta})$, where θ is a user-defined threshold that is set to be 0.1 throughout this work.

We consider the following two adaptive refinement strategies depending on the type of initial mesh. For quadrilateral meshes, we adopt an adaptive refinement scheme as shown in Fig. 1(b). In this scheme, each marked element is subdivided into several quadrilateral elements by connecting the midpoint of each edge to its centroid. For polygonal (e.g., CVT) meshes, we use the adaptive refinement scheme shown in Fig. 1(c), where we subdivide each marked element with n vertices into $n+1$ CVT elements using Lloyd's algorithm. The initial seeds of Lloyd's algorithm are placed at the centroid of the element as well as the midpoints of the lines connecting the centroid and the vertices [39].

To effectively store the hierarchical information in the mesh refinement, we adopt the PolyTree data representation introduced in [39,41], as illustrated in Fig. 2. To distinguish the elements with different levels of refinement, we categorize the mesh into different levels. For instance, all the elements in the initial mesh belong to level 0, and an element obtained after two subdivisions belongs to level 2. Moreover, at a given level, if an element is being subdivided, we refer to it as a "parent" element and we refer to those elements obtained from the subdivision as the "children" elements, which belong to the next level. With this data representation, for any given element in the mesh, we can easily access which refinement level it belongs to and which element is its parent, both of which are essential to the adaptive coarsening scheme that is described in the following subsection.

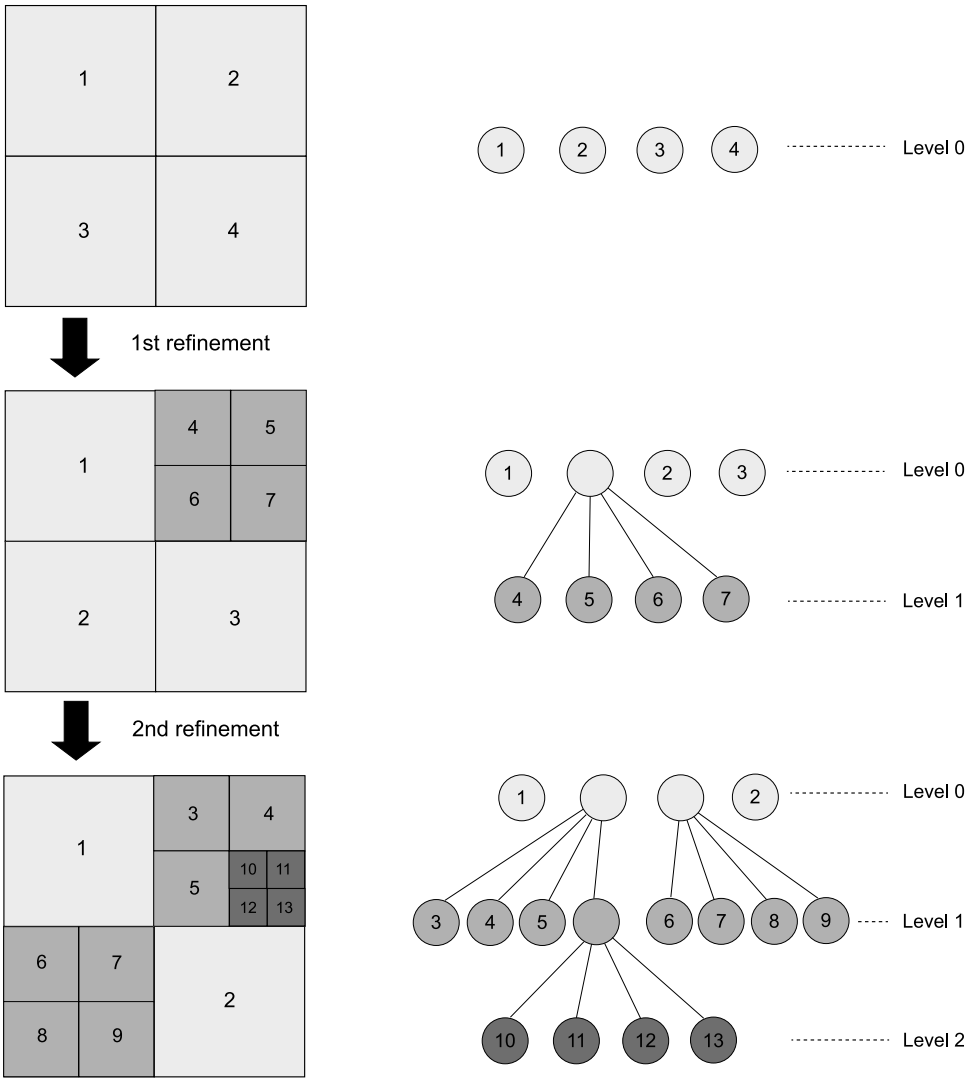

Fig. 2. A schematic illustration of two successive refinement processes on a quadrilateral mesh and the corresponding PolyTree data representation of element numbering.

7.2. Adaptive coarsening

Adaptive coarsening is essential for computational efficiency, because the design field is constantly changing throughout the optimization, and regions that were once fully dense may become void in later steps and no longer need such a refined discretization. To that end, this work also introduces an adaptive coarsening strategy in conjunction with the adaptive refinement.

The basic idea of the adaptive coarsening is to de-refine the "children" elements with the same densities back to their parents. If we identify that all of the "children" elements of a "parent" element have the same (under a tolerance, e.g. 10^{-4}) material density (namely, *filtered design variable*[2]) for every candidate material, we then replace these "children" elements with the "parent" one. In practice, we start this process for all the elements in

[2] Notice that, in the adaptive coarsening scheme, we monitor the filtered design variables instead of the unfiltered design variable because we do not want the coarsening to affect the density filter.

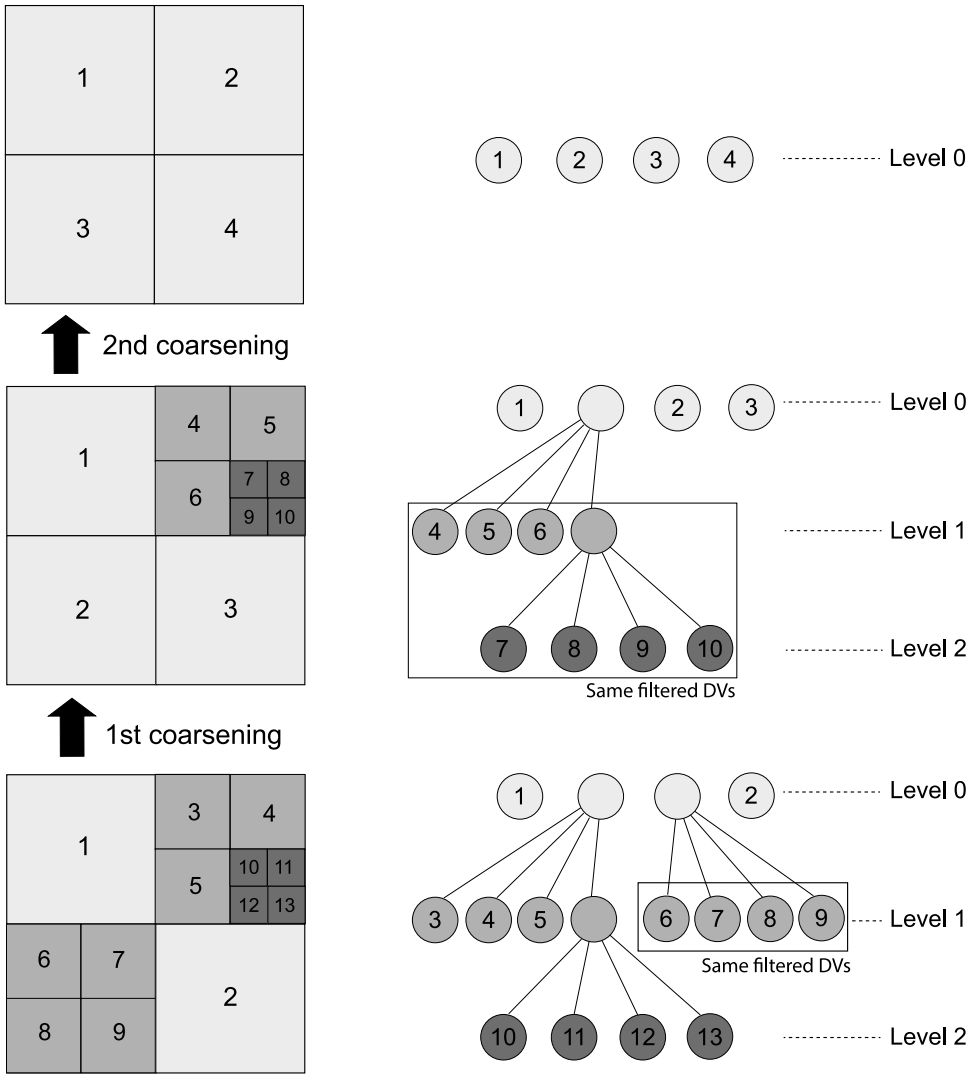

Fig. 3. A schematic illustration of two successive coarsening processes on a quadrilateral mesh and the corresponding PolyTree data representation of element numbering.

the highest level of the Polytree data structure, and gradually move down in terms of the level until we reach level 0 (i.e., the coarsest level). An illustration of this coarsening procedure is provided in Fig. 3.

7.3. Mapping of design variables

A crucial step to ensure the effectiveness of the adaptive refinement and coarsening schemes are the mapping of design variables. In this work, the mapping of the displacement field is not needed because the adaptive refinement and coarsening are done only between optimization steps.

We map the design variables as follows. In the adaptive refinement, if we subdivide an element into a set of "children" elements, the *unfiltered design variables* of those "children" elements are set to be equal to the *unfiltered design variable* of the "parent" element. Similarly, when a set of "children" elements is coarsened to their "parent" element, the *unfiltered design variable* of the coarsened element is taken to be the *unfiltered design variables* of those "children" elements.

We use $\boldsymbol{\rho}_i^{new}$ to denote the vector of mapped unfiltered design variables for material i on the new mesh. Once $\boldsymbol{\rho}_i^{new}$ is obtained, the vector of filtered design variables for material i, denoted as $\overline{\boldsymbol{\rho}}_i^{new}$, is computed as

$$\overline{\boldsymbol{\rho}}_i^{new} = \left(\mathbf{P}_i^{new}\right)\boldsymbol{\rho}_i^{new}, \tag{87}$$

where $\mathbf{P}_i^{new}$ is the density filter matrix formed on the new mesh for material i.

8. Numerical examples

In this section, we present four numerical examples (three for maximizing the potential energy at equilibrium states and one for compliant mechanism design) to demonstrate the efficiency and effectiveness of the proposed VEM-based topology optimization formulation considering multiple types of hyperelastic materials (i.e., modified Saint Venant-Kirchhoff model, compressible Ogden model, and porous elastomers with Neo-Hookean matrix).

Throughout this section, the Modified Generalized Displacement Control (MGDC) approach [88] is adopted to perform nonlinear structural analysis at each optimization step with an initial load factor of $\Delta\lambda = 0.5$. The convergence tolerance of the norm of the residual vector is set to be 10^{-3}. If the solution cannot converge at a certain optimization step, we then recursively reduce the initial load factor $\Delta\lambda$ by half and perform the structural analysis until convergence is achieved. In terms of the optimization parameters, we set the move limit and damping ratio in the modified ZPR design update scheme to be $move = 0.1$ and $\eta = 0.5$, respectively. To calculate the energy interpolation factor γ_e, the threshold ρ_0 is chosen according to the following continuation formula: $\rho_0 = \underline{\rho}_0 + (3-p)(\overline{\rho}_0 - \underline{\rho}_0)/2$, where $\overline{\rho}_0$ (taken to be 0.008 here) and $\underline{\rho}_0$ (taken to be 0.004 here) are the upper and lower bounds of ρ_0 and p is the SIMP penalization parameter. According to the above formula, as p gradually increases from 1 to 3, the threshold ρ_0 reduces linearly from its upper bound $\overline{\rho}_0$ to its lower bound $\underline{\rho}_0$. A continuation of the density filter radius R is adopted as well. For the first three examples, the filter radius for each candidate material is initially set as $R = R_0$ and is then reduced every 5 optimization steps by $\Delta R = -7R_0/160$ starting from optimization step 80 until R reaches $R = R_0/8$. For the fourth example, the filter radius for each candidate material is initially set as $R_0 = 0.125$ and is then reduced every 5 optimization steps by $\Delta R = -0.004$ starting from optimization step 70 until R reaches $R = 0.045$. All the numerical examples use uniform initial guesses for each of the candidate materials (for example, if the total volume fraction is $\sum_{j=1}^{nc} V_{\max}^j = 0.4$ and a total of $m = 4$ materials are assumed, the initial design variable value for each material is 0.1).[3]

8.1. Example 1: cantilever beam design with Ogden-based model subjected to end load

In the first example, we consider the design of a cantilever beam subjected to a downward end load F. The dimensions, boundary, and loading conditions of the design domain are shown in Fig. 4(a). To investigate the influence of the load level on the layout of the final design, three values of F are considered, namely, $F = 10, 20,$ and 40. Additionally, to showcase the capability of the proposed material interpolation scheme in handling any number of candidate hyperelastic materials, this example considers three design cases with different numbers (i.e., two, four, and eight) of one-term (i.e. $N_O = 1$) Ogden materials and assigns one individual volume constraint to each candidate material. The material parameters (m_α, Young's Modulus E_0, and Poisson's ratio v) for each candidate material associated with each design case are given in Table 1. The nonlinear elastic response of those candidate materials (i.e., stretch vs. first PK stress) under uniaxial tension is shown in Fig. 4(b)–(d).

The additional setup of parameters for the optimization and adaptive VEM analysis in this example are summarized as follows. In terms of optimization, the initial filter radius R_0 is chosen to be $R_0 = 0.125$ for all the candidate materials and we adopt a continuation scheme on SIMP penalization parameter p as follows: (*i*) For the case of two candidate materials, p is initially set to 1 and is increased by $\Delta p = 0.15$ every optimization step until $p = 3$ is reached; (*ii*) for the case of four candidate materials, p is initially set to 1 and is increased by $\Delta p = 0.2$ every 2 optimization steps until $p = 3$ is reached; and (*iii*) for the case of eight candidate materials, p is initially set to 1 and is increased (starting at optimization step 10) by $\Delta p = 0.1$ every 2 optimization steps until $p = 3$ is reached. We remark that less aggressive continuation schemes on p are adopted for design cases with more candidate materials because, similar to the original DMO scheme, the proposed DMO-type material interpolation

[3] The examples in this section are carried out on a desktop computer with an Intel(R) Xeon(R), 3.00 GHz processor (8 cores), and 256 GB of RAM running Matlab R2018b.

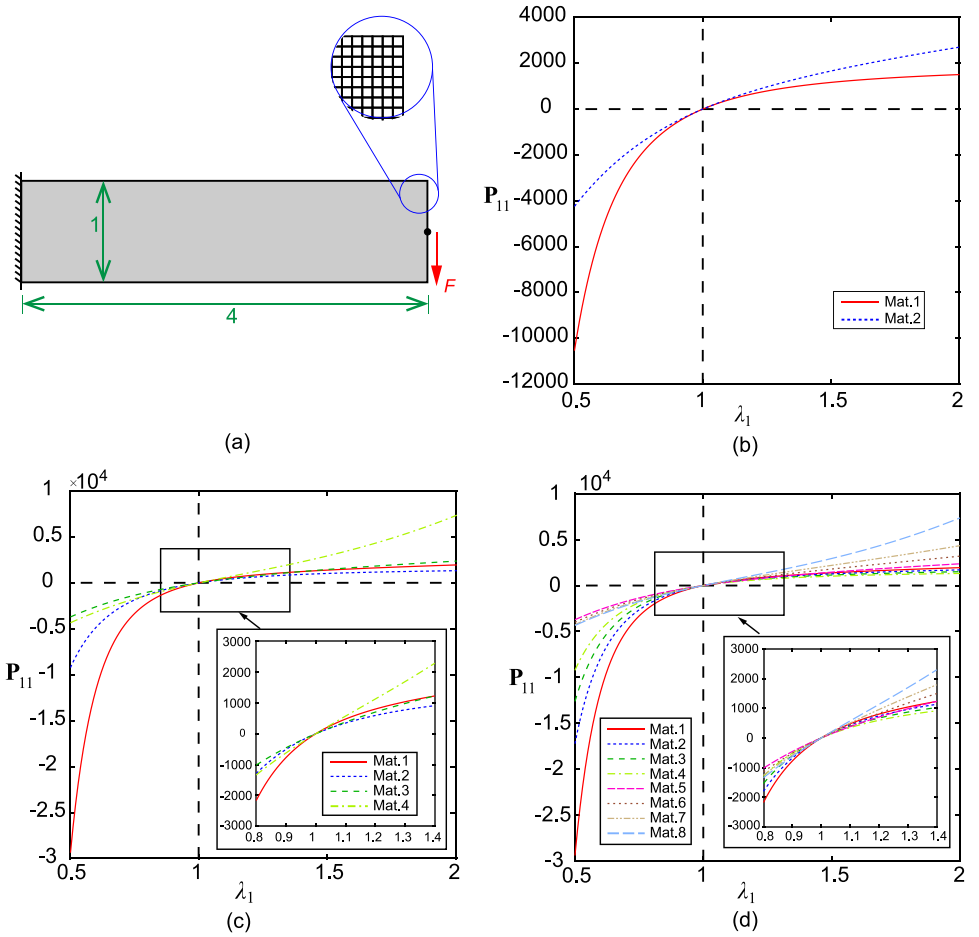

Fig. 4. (a) Dimensions, load, and boundary conditions of the design domain for Example 1. The nonlinear elastic responses (i.e., stretch vs. first PK stress) of (b) two candidate Ogden materials under uniaxial tension; (c) four candidate Ogden materials under uniaxial tension; (d) eight candidate Ogden materials under uniaxial tension. The material properties of those materials in (b) – (d) are provided in Table 1.

Table 1
Properties of Ogden-based candidate materials and their individual volume fractions considered in Example 1.

# of Mats.		Mat. 1	Mat. 2	Mat. 3	Mat. 4	Mat. 5	Mat. 6	Mat. 7	Mat. 8
Two	m_1	2	−2						
	E_0	4000	4000						
	v	0.35	0.35						
	$V^j_{\max}$	0.25	0.25						
Four	m_1	−4	−2	2	4				
	E_0	5000	3500	3500	5000				
	v	0.35	0.35	0.35	0.35				
	$V^j_{\max}$	0.125	0.125	0.125	0.125				
Eight	m_1	−4	−3	−2.5	−2	2	2.5	3	4
	E_0	5000	4500	4000	3500	3500	4000	4500	5000
	v	0.35	0.35	0.35	0.35	0.35	0.35	0.35	0.35
	$V^j_{\max}$	0.0625	0.0625	0.0625	0.0625	0.0625	0.0625	0.0625	0.0625

Table 2
Summary of the total computational time and the final objective values obtained by the improved ZPR (Section 6) and MMA over 200 optimization steps and under $F = 10$.

# of candidate Mats.		Two	Four	Eight
ZPR	Wall clock time (s)	9.44	19.74	40.52
	Final objective	3.80	3.39	3.46
MMA	Wall clock time (s)	398.15	570.41	1937
	Final objective	3.77	3.40	3.44

Table 3
Summary of the total computational time and the final objective values obtained by VEM with an adaptively refined and coarsened mesh and a uniform mesh with $F = 10$ [4].

# of candidate Mats.		Two	Four	Eight
VEM + adap. refinement & coarsening	Wall clock time (s)	8237	6736	12 424
	Final obj.	3.80	3.39	3.46
VEM + uniform mesh	Wall clock time (s)	18 647	30 500	56 964
	Final obj.	3.82	3.39	3.52

scheme (i.e., Eq. (40)) exhibits slow convergence in the first few optimization steps for uniform initial guesses when the number of candidate materials is large.

In terms of the adaptive VEM analysis, we initially discretize the design domain into a mesh of 104×26 structured quadrilateral elements and adopt the adaptive refinement and coarsening scheme introduced in Section 7 as the optimization progresses. For design cases with two, four, and eight candidate materials, the adaptive refinement starts at optimization step 20, 30, and 50, respectively, and is performed every 10 optimization steps afterward based on the criteria described in Section 7. The adaptive coarsening is performed every 3 optimization steps after the first adaptive refinement. Additionally, for all the design cases considered, we set the maximum refinement level to 1 before optimization step 130 and then increase the allowable refinement level to 2 afterwards.

Before we present the results for all the load levels, we first restrict our attention to the smallest load level, $F = 10$, and showcase the efficiency and effectiveness of the modified ZPR update scheme in Section 6 by comparing its performance with that of the commonly-used MMA method [65]. The comparison of the total computational time spent by the modified ZPR design update scheme and the MMA, together with the final values of the objective function, are summarized in Table 2 for the design cases with two, four, and eight candidate materials, respectively. We observe that, while achieving almost identical objective values, the ZPR, as a tailored design update scheme for multi-material topology optimization, is more computationally efficient than MMA (which is a general-purpose design update scheme); and the speedup increases as the number of candidate materials increases. This is because the update of the design variables associated with each candidate material (and its individual volume constraint) is separated and performed in parallel in the ZPR update scheme, whereas the update of all the design variables for all the candidate materials are done together in MMA.

Furthermore, we also demonstrate the computational efficiency of the adaptive refinement and coarsening scheme by comparing its performance with that of a uniform mesh. Similarly, we set the load level to be $F = 10$. For a fair comparison, we consider a uniform discretization of the design domain into a 416×104 structured quadrilateral mesh, which results in the same "design resolution" as the adaptively refined and coarsened one with an initial 104×26 grid and two refinement levels. In Table 3, we present the computational time spent by the VEM analysis on the adaptively refined and coarsened mesh and the uniform one together with the final objective values obtained in the different design cases. We can see that, by employing the proposed adaptive mesh refinement and coarsening scheme, the total computational time in the VEM analysis is significantly reduced without loss of accuracy. As illustrated in Fig. 5 together with several snapshots of the deformed meshes in a few optimization steps, the considerable computational time reduction is mainly caused by the greatly reduced number of nodes in

[4] The computation in forming the nonlinear system of equations (i.e. stiffness matrix and internal force vector) and computing the sensitivities are paralleled in 4 cores throughout the optimization process. The inverse is performed using the backslash operator in Matlab.

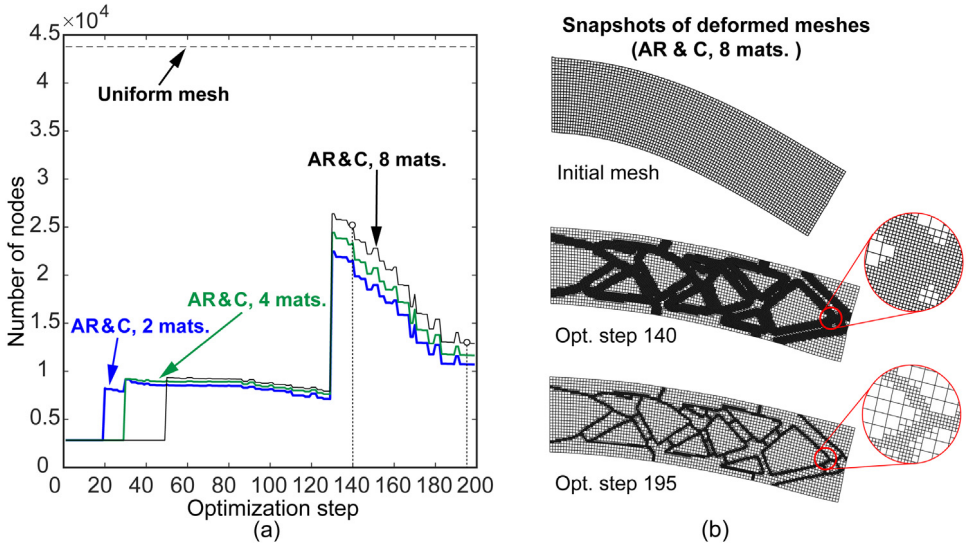

Fig. 5. (a) Evolution of the number of nodes in the adaptively refined & coarsened (AR&C) and the uniform meshes throughout the optimization history for design cases with two, four, and eight candidate materials and $F = 10$. (b) Several snapshots of the deformed adaptively refined & coarsened mesh in the design case with eight candidate materials.

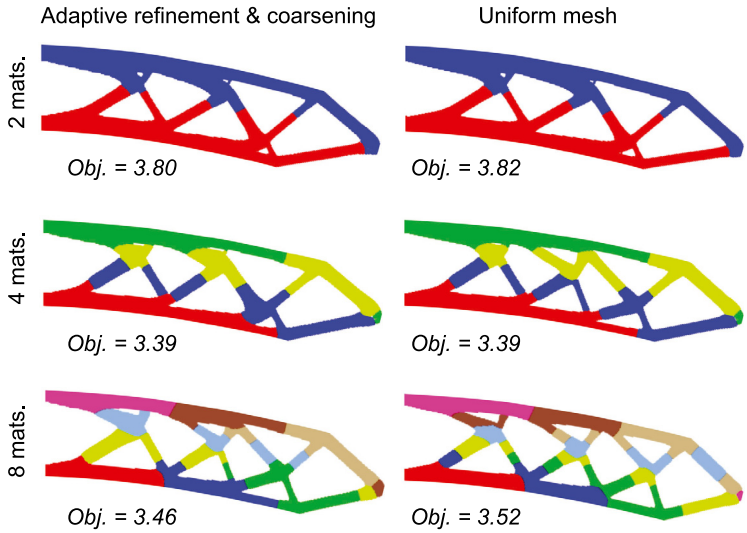

Fig. 6. Comparison of final topologies obtained on an adaptively refined & coarsened mesh and a uniform mesh considering two (top row), four (middle row), and eight (bottom row) candidate materials under $F = 10$. The adaptively refined & coarsened and the uniform meshes have the same spatial resolution. The CPU comparison of results with and without mesh adaptivity are provided in Table 3.

the adaptively refined and coarsened mesh as compared to the uniform mesh throughout the optimization history. Additionally, we plot in Fig. 6 the final topologies for the cases of two, four, and eight candidate materials. We observe that, for the designs in all the cases, the stiffer materials are placed in the outer regions of the designs while the more compliant ones are placed toward the middle region. In addition, the materials that are stiff in tension are placed in the upper part and the ones that are stiff in compression are assigned to the lower part. Those observed features suggest that the proposed multi-material topology optimization framework and the improved ZPR update scheme can effectively distribute materials in the optimized configuration according to their respective nonlinear behavior. Moreover, according to the comparisons in the figure, both the adaptively refined and coarsened mesh and the uniform mesh produce almost identical designs as well as material distributions when there are two candidate

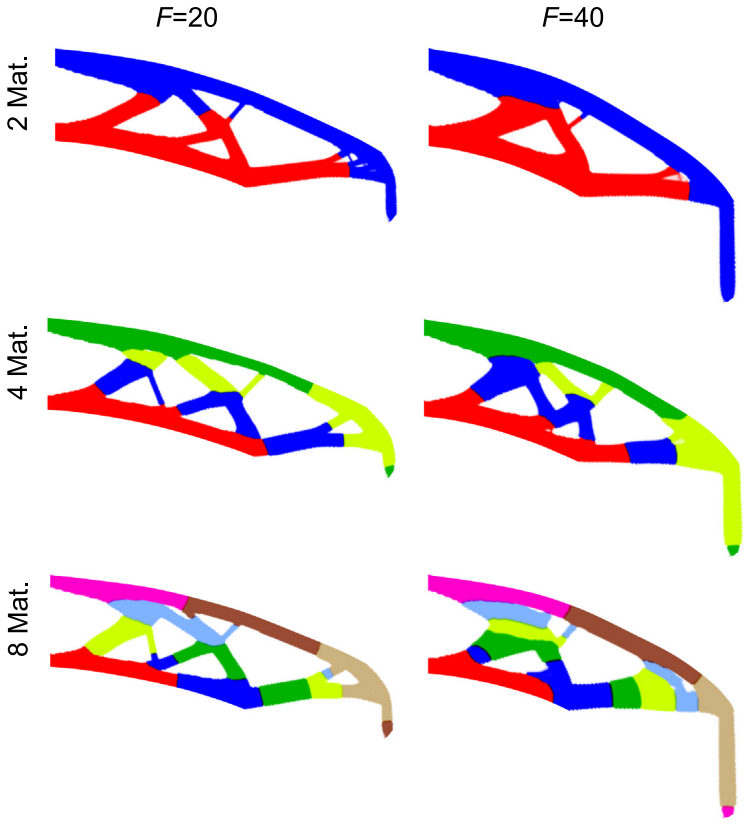

Fig. 7. Deformed configurations of optimized designs obtained with two, four, and eight candidate materials under higher load levels (i.e., $F = 20$ and 40).

materials. However, as the number of candidate materials increases to four and eight, the adaptively refined and coarsened mesh and the uniform mesh produce distinct structural layouts as well as different material distributions, but have almost identical final objective values. This suggests that, because this optimization problem with a large number of materials is highly non-convex, the two cases converge to different local minima.

Having demonstrated the computational efficiency of the modified ZPR design update scheme (Section 6) and the adaptive mesh refinement and coarsening strategies (Section 7), we now present in Fig. 7 the final topologies obtained from the proposed VEM-based multi-material topology optimization framework under higher load levels (i.e., $F = 20$ and 40) when considering multiple Ogden materials (i.e., two, four, and eight). As shown from the figure, the proposed topology optimization framework is able to capture the influence of the load level on the final topologies when multiple hyperelastic materials are present. Additionally, the deformed configurations of the designs obtained for cases of $F = 40$ indicate the multi-material topology optimization framework together with the energy interpolation scheme [6] is robust and able to simulate large deformation responses well.

8.2. Example 2: double clamped beam design with Ogden-based and Saint-Venant models

In the second example, we consider the double clamped beam design, which is a benchmark problem in the literature of topology optimization under large deformations [30]. As illustrated in Fig. 8(a), the design domain of dimensions 4×1 is fixed on both sides and is subjected to a downward distributed load of magnitude τ in the middle of its top side.

The setups of the optimization and VEM analysis of this example are described as follows. In the optimization, we initialize p as 1 and then increase it by $\Delta p = 0.2$ every 2 optimization steps until we reach $p = 3$. The initial filter radius is set to $R_0 = 0.1$. In the VEM analysis, we consider the left half of the design domain because

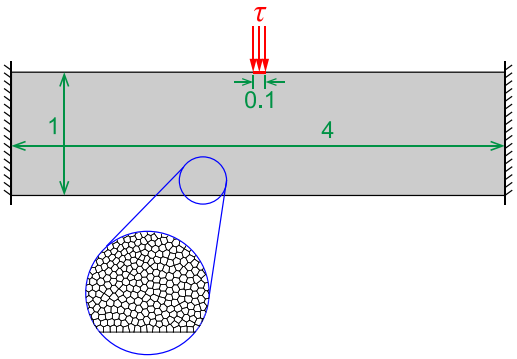

(a)

n	n-gon	# of n-gons
4		39
5		1,139
6		3,147
7		668
8		7
# of Elements		5,000

(b)

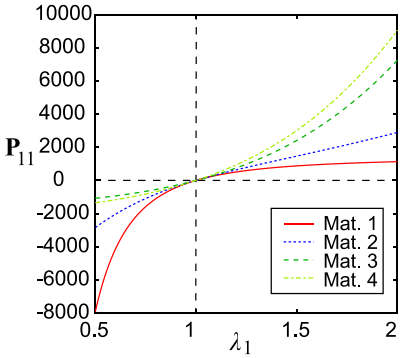

(c)

Fig. 8. (a) Dimensions, load, and boundary conditions of the design domain for Example 2. (b) A statistics of the CVT mesh considered. (c) The nonlinear elastic response (i.e., stretch vs. first PK stress) of the four candidate materials (i.e., two Ogden and two Saint-Venant materials) under uniaxial tension. The material properties of the candidate materials are provided in Table 4.

Table 4
Properties of the candidate materials and the volume fractions in each constraint scenario considered in Example 2.

	Mat. 1	Mat. 2	Mat. 3	Mat. 4
Type	Ogden	Ogden	Saint-Venant	Saint-Venant
E_0	3000	3000	3200	4000
v	0.35	0.35	0.35	0.35
m_1	-2	3		
Constraint scenario 1 ($V^j_{\max}$)	0.06	0.14/3	0.14/3	0.14/3
Constraint scenario 2 ($V^j_{\max}$)	0.06		0.14	

of structural symmetry and discretize it with an initial CVT mesh of 5000 polygonal elements. The statistics of the initial mesh are summarized in Fig. 8(b). Beginning from optimization step 30, the adaptive refinement and coarsening schemes are performed every 10 and 3 optimization steps, respectively. The maximum refinement level is taken to be 1 before optimization step 160 and to be 2 afterwards.

To showcase the capability of the proposed material interpolation scheme in handling a combination of different types of hyperelastic materials, this example considers four candidate materials — two characterized by the Ogden model and the other two by the Saint-Venant model. The material parameters of these four candidate materials are summarized in Table 4 and their stress–stretch relationships under uniaxial tension are plotted in Fig. 8(c). Additionally, two volume constraint scenarios are studied. The first scenario assigns an individual volume constraint to each candidate material (i.e., $nc = 4$) and, in the second scenario, material # 1 is assigned with an individual volume constraint and materials # 2, 3, and 4 are assigned with a collective volume constraint (i.e., $nc = 2$). The details of these two volume constraint scenarios are summarized in Table 4.

We consider two values of load level τ in this example, namely $\tau = 10$ and $\tau = 300$. For both smaller and larger τ values, Fig. 9(a) and (b) plot the optimized designs obtained with constraint scenario 1 (i.e., each candidate material is assigned with an individual volume constraint) and scenario 2 (i.e., material # 1 is assigned with an individual constraint and materials # 2–4 are assigned with a collective one), respectively. Additionally, Fig. 10(a) and (b) respectively show the convergence history of the objective functions in constraint scenarios 1 and 2 for the larger τ value. From both figures, we conclude that the proposed framework can deliver smooth convergence and is capable of capturing the influence of the load level in the design when various types of candidate materials are present. For the smaller τ value, because all the candidate materials behave in the linear elastic regime, the framework produces designs which resemble the ones obtained by topology optimization considering multiple linear elastic materials. On the other hand, for the larger τ value, because each candidate material behaves in their respectively nonlinear regime, the framework yields designs which are distinctive from the ones obtained by considering linear elastic materials. The designs obtained with the larger τ are less prone to snap-through behavior [30]. Moreover, the

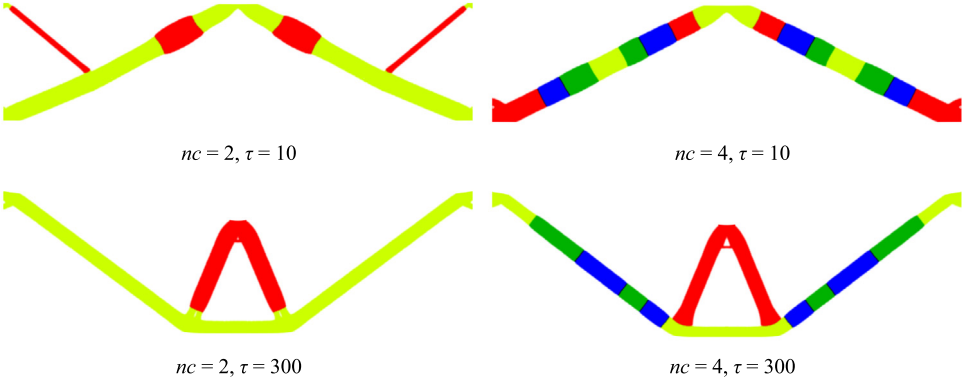

Fig. 9. Deformed configurations of the final designs under different load levels (i.e., $\tau = 10$ and $\tau = 300$) and volume constraint settings (i.e., $nc = 2$ and $nc = 4$ according to Table 4).

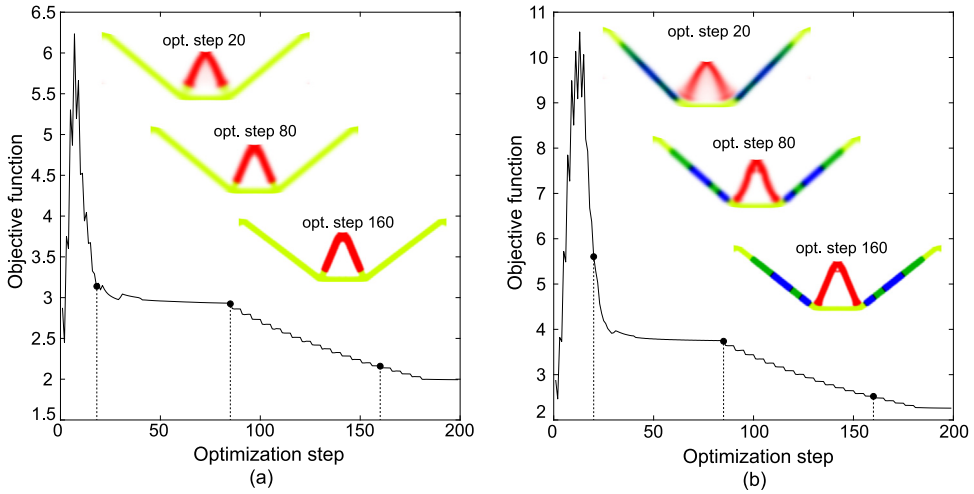

Fig. 10. The convergence history of the objective function with snapshots of the intermediate designs for (a) the case of $\tau = 300$ and $nc = 2$; and (b) the case of $\tau = 300$ and $nc = 4$.

results demonstrate that the proposed framework is able to distribute each candidate material in the most appropriate locations of the final design according to their respective nonlinear behavior. For instance, because candidate material #1 is the stiffest in compression (see Fig. 8(c)), it is assigned to the compressive members in the final designs. In addition, because material #4 has the stiffest tensile response (see Fig. 8(c)), it is chosen in the second constraint scenario by the proposed optimization framework among materials #2 – #4 to be assigned to the tensile members in the final designs.

8.3. Example 3: multiple load cases design with porous elastomers

In the third example, we aim to demonstrate that the proposed framework is readily extendable to account for multiple load cases [64,89] and other stored-energy functions derived from the homogenization theory. To that end, we consider a design domain shown in Fig. 11(a) which are subjected to a set of two linearly independent load cases. Five porous elastomers with different porosities are considered as candidate materials in this design example, whose stored-energy function is given in (11). The material parameters and the nonlinear elastic response of the 5 porous elastomers are shown in Table 5 and Fig. 11(c), respectively. In this design example, each candidate material is assigned to an individual volume constraint of $V^j_{\max} = 0.04$, which leads to a total of volume fraction of 20%.

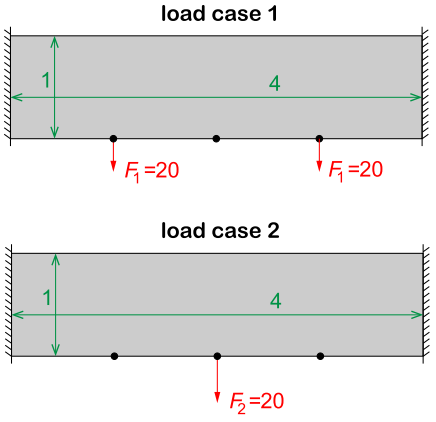

(a)

n	n-gon	# of n-gons
4		31
5		1,154
6		3,143
7		664
8		9
# of Elements		5,000

(b)

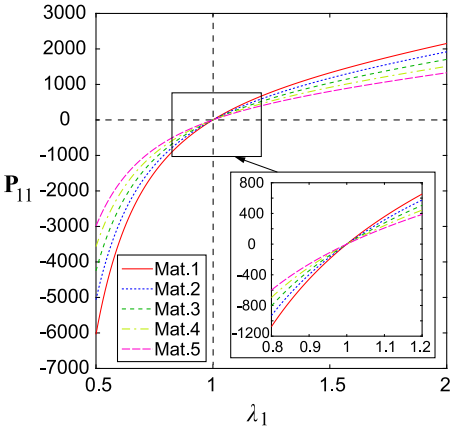

(c)

Fig. 11. (a) Dimensions, load, and boundary conditions of the design domain for Example 3. (b) A statistics of the CVT mesh considered. (c) The nonlinear elastic response (i.e., stretch vs. first PK stress) of the 5 candidate porous elastomers under uniaxial tension. The material properties and porosities of the porous elastomers are provided in Table 5.

Table 5
Properties of the candidate porous elastomers considered in Example 3.

# of candidate Mats.	Mat. 1	Mat. 2	Mat. 3	Mat. 4	Mat. 5
μ	2000	2000	2000	2000	2000
f_0	0.25	0.3	0.35	0.4	0.45

Similarly to the second design example, parameter p is initialized from 1 and is then increased by $\Delta p = 0.2$ every 2 optimization steps until reaching $p = 3$; and $R_0 = 0.1$. Regarding the VEM analysis, we consider the left half of the design domain and introduce an initial CVT discretization with 5000 elements. The statistics of the CVT mesh are summarized in Fig. 11(b). Beginning from optimization step 30, the adaptive refinement and coarsening schemes are performed every 10 and 3 optimization steps, respectively. The maximum refinement level is taken to be 1 before optimization step 160 and to be 2 afterward.

In Fig. 12(a), the final design is depicted together with its deformed configuration under two load cases. Additionally, Fig. 12(b) shows the convergence history of the objective function for this design problem. From both figures, we can conclude that the proposed framework is effective in handling multiple porous elastomers with a wide range of porosities, accounting for multiple load cases, and converging smoothly.

8.4. Example 4: compliant mechanism design with Ogden-based model

In the last design example, we deploy the proposed framework to compliant mechanism design (see Section 5.5) to demonstrate its generality. The domain and boundary conditions of the design problem are shown in Fig. 13(a). An input force of magnitude $F = 340$ is applied to the middle of the left edge of the design domain, and we aim to maximize the output displacement in the negative y direction. The stiffness of the springs k_{in} and k_{out} are chosen as $k_{in} = 800$ and $k_{out} = 30$, respectively. Because of symmetry, only the lower half design domain is considered and is discretized with an initial CVT mesh of 6000 elements, whose statistics are listed in Fig. 13(b). Four Ogden materials are considered, whose material parameters and nonlinear elastic responses under uniaxial tension are shown in Table 6 and Fig. 13(c). In this design example, a total volume constraint of 20% is assigned to all the materials. During optimization, we fix the SIMP penalization parameter to be 3. Beginning from optimization step 40, the adaptive refinement is performed every 10 steps and the adaptive coarsening is performed every 3 steps. Throughout the optimization process, we allow for one refinement level.[5]

[5] We only allow for one refinement level in order to avoid the formation of very thin hinge connections in the final design with a high-resolution mesh. To address this issue, the robust formulation [90] could be adopted.

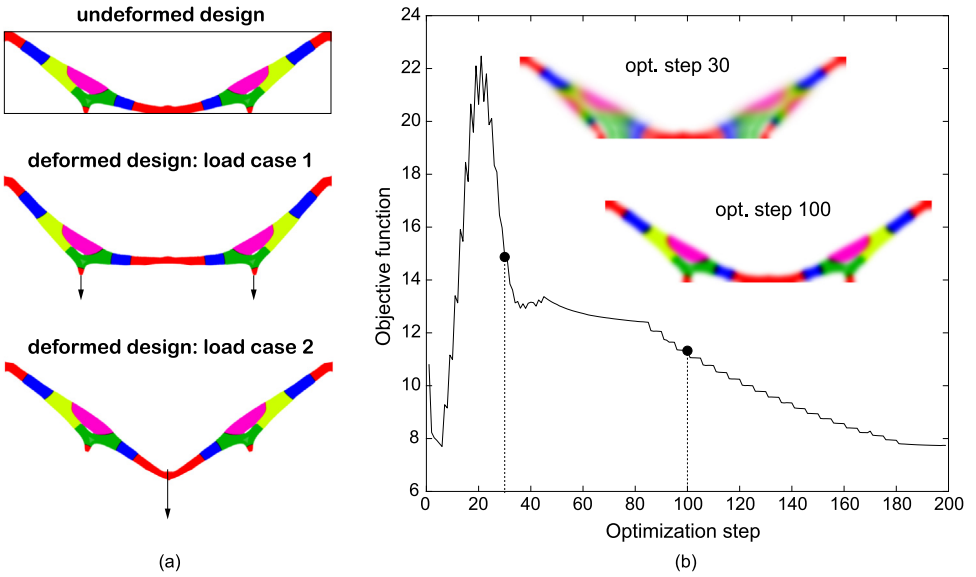

Fig. 12. (a) Undeformed and deformed configurations of the final design under two load cases. (b) Convergence history of the objective functions with snapshots of the intermediate designs.

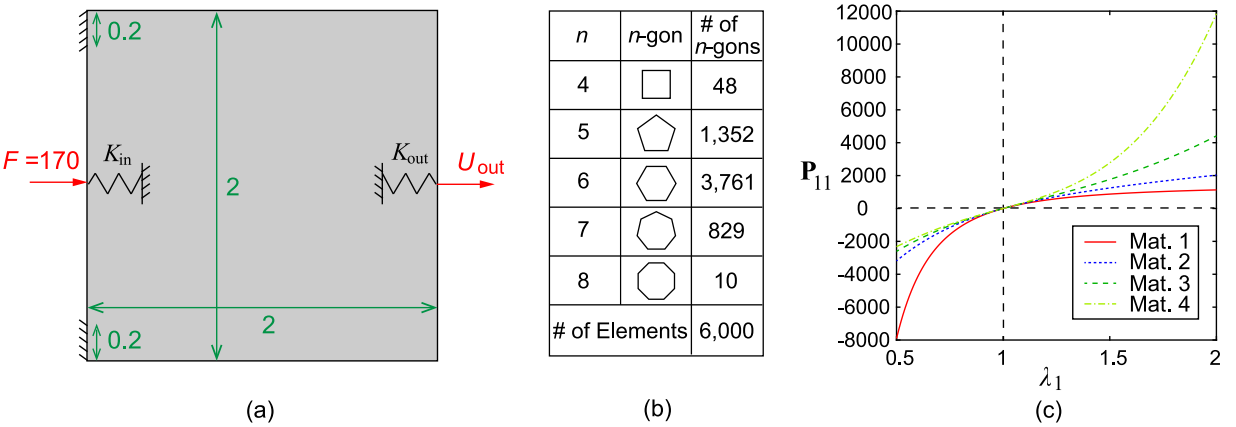

Fig. 13. (a) Dimensions, load, and boundary conditions of the domain for the compliant mechanism design. (b) A statistics of the CVT mesh considered. (c) The nonlinear elastic response (i.e., stretch vs. first PK stress) of the 4 candidate Ogden-based materials. The material properties are provided in Table 6.

Table 6
Properties of the candidate Ogden materials considered in Example 4.

# of candidate Mats.	Mat. 1	Mat. 2	Mat. 3	Mat. 4
m_1	−2	2	4	6
E_0	3000	3000	3000	3000
v	0.35	0.35	0.35	0.35

The final compliant mechanism design is shown in the undeformed and deformed configurations in Fig. 14(a) and (b), respectively. It can be seen from the figure that the framework assigns materials #1 and #4, which are the stiffest in compression and tension, respectively (see Fig. 13(c)), to those members in the final design that are under compression and tension, respectively. Materials #2 and #3 are not assigned in the final design, because they are less efficient in terms of material properties (thus less favorable under one global volume constraint setting).

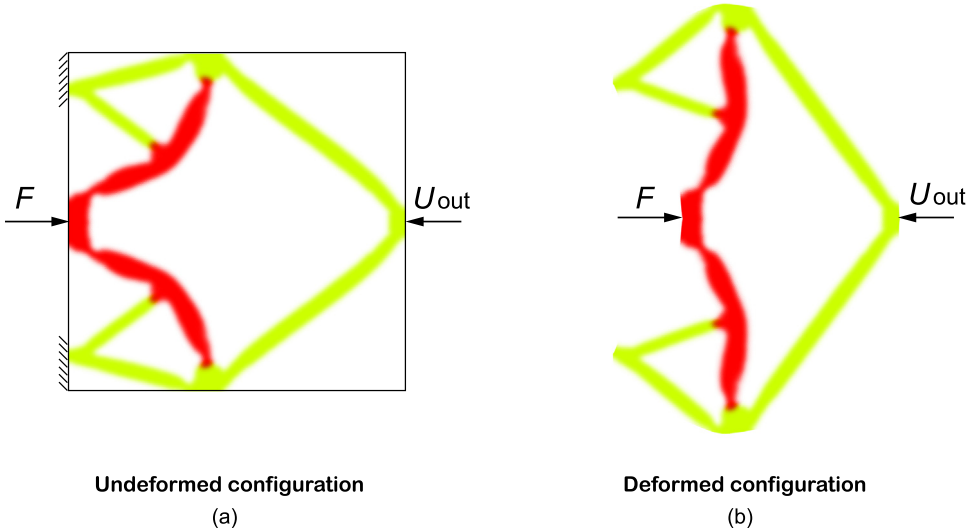

Fig. 14. The final compliant mechanism design obtained from the proposed work shown in (a) undeformed configuration and (b) deformed configuration. The magnitude of the output displacement U_{out} is 0.3 in the final design.

We also note that all the candidate materials have the same Young's modulus and Poisson's ratio, therefore, a multi-material formulation considering linear elasticity cannot assign these four materials properly because they behave identically in the linear elastic regime. This example demonstrates that the proposed framework is effective in distributing multiple candidate hyperelastic materials in proper regions in the final design according to their nonlinear elastic behaviors.

9. Concluding remarks

This work presents a VEM-based multi-material topology optimization framework considering finite deformations. A material interpolation scheme is presented, which is shown to be effective in handling an arbitrary number of hyperelastic materials characterized by various stored-energy functions. We demonstrate three nonlinear material models, which are the modified Saint Venant-Kirchhoff model, the compressible Ogden model, and porous elastomers with Neo-Hookean matrix. An energy interpolation scheme is introduced, which extends the one by Wang et al. [6] to account for multiple candidate materials. This energy interpolation scheme is shown to alleviate the excessive distortion and numerical instability of low-density elements and to stabilize the convergence of the structural solver under large deformations. The proposed framework introduces adaptive VEM and modified ZPR (with parallel computing) to improve the computational efficiency of both the nonlinear structural analysis and optimization updates. On the structural analysis side, the lower-order VEM, which does not need any numerical integration to construct the element-level stiffness matrix and internal force vector, is adopted in approximating and solving the nonlinear structural systems. Compared to the FEM approximation, the VEM can effectively reduce the total number of function evaluations when forming the multi-material system and, comparatively, more reduction can be achieved with more candidate materials. The VEM has a unique ability to handle arbitrary element shapes, which is exploited to perform adaptive mesh refinement and coarsening strategies by reducing the size of the structural system of equations while maintaining the spatial resolution of the design. On the optimization side, the modified ZPR design update scheme which handles both negative and positive sensitivities of the objective function is derived in the present framework to efficiently update the design variables associated with each constraint in parallel.

Four design examples are presented to showcase the effectiveness and efficiency of the proposed framework in various design scenarios and with different types of hyperelastic materials. In the first example, we consider a cantilever design with various numbers of Ogden-based materials and demonstrate that the proposed framework is robust with respect to large deformations. In the meantime, this example also showcases the computational efficiency of both the modified ZPR design variable update scheme and the adaptive mesh refinement and coarsening

strategies by comparing them with the MMA and a uniform mesh, respectively. For example, when eight candidate materials are present, around 40 times and 5 times speedup are achieved in the design update and the nonlinear structural analysis, respectively, without loss of accuracy. In the second example, we consider the classical double clamped beam design with four candidate materials: two Ogden-based materials and two Saint-Venant materials. The results indicate that the proposed framework can capture the influence of different load levels on the final design, and the proposed material interpolation scheme can simultaneously work with different types of hyperelastic candidate materials. In the third example, we consider a multiple-load-case design problem with five porous elastomers of various porosities. The results suggest that the proposed framework can effectively handle not only multiple materials with classical hyperelastic models but also multiple soft composite materials whose stored-energy functions are derived from the homogenization theory. In the last example, a compliant mechanism design is presented with four Ogden-based materials and a global volume constraint, showcasing the effectiveness of the proposed framework in properly distributing multiple hyperelastic materials in the final design according to their respective nonlinear elastic behavior under large deformations.

Declaration of competing interest

The authors declare that they have no known competing financial interests or personal relationships that could have appeared to influence the work reported in this paper.

Acknowledgments

This paper is dedicated to the memory of Dr. Joakim Petersson (1968–2002). We appreciate the useful discussions and suggestions from Mrs. Emily D. Sanders, which contributed to substantially improve this manuscript. X. S. Zhang would like to acknowledge the financial support from the start-up fund at the University of Illinois at Urbana-Champaign, United States. The work by G. H. Paulino and H. Chi are supported in part by the endowment provided by the Raymond Allen Jones Chair at the Georgia Institute of Technology, United States. The information provided in this paper is the sole opinion of the authors and does not necessarily reflect the view of the sponsoring agencies.

Appendix. FE approximation of the potential energy functional in (48)

Instead of using the virtual element approximation of the potential energy, one can also adopt a FE approximation of the potential energy functional (48). The material interpolation and energy interpolation schemes introduced in Section 5.2 are both valid in either case.

More specifically, if we were to approximate (48) with FEM, the approximation takes the following form:

$$\begin{aligned}\Pi_h^{FEM}(\boldsymbol{\rho}_1,\ldots,\boldsymbol{\rho}_m,\boldsymbol{\gamma},\mathbf{v}_h) = \sum_{E^{(e)}\in\Omega_h}\Bigg\{ &\sum_{i=1}^{m}\Big[w_i\Big(\overline{\rho}_1^{(e)},\ldots,\overline{\rho}_m^{(e)}\Big)\fint_{E^{(e)}} W_i\Big(\mathbf{C}(\gamma^{(e)}\mathbf{v}_h)\Big)\mathrm{d}\mathbf{X}\Big] \\ &+\Big(1-(\gamma^{(e)})^2\Big)\fint_{E^{(e)}} W^{L,\rho}(\rho_1^{(e)},\ldots,\rho_m^{(e)},\mathbf{v}_h)\Bigg\} - \langle\mathbf{t},\mathbf{v}_h\rangle_h, \end{aligned} \tag{88}$$

where $\fint_E(\cdot)$ stands for the numerical integration on a generic element E and $\langle\mathbf{t},\mathbf{v}_h\rangle_h$ is the standard FE approximation of the loading term. If we specify $\mathbf{X}_E^Q$, $Q=1,\ldots,N_E^Q$ as the quadrature points of $\fint_E(\cdot)$ over element domain E and w_E^Q as the corresponding weights [91], we can further express the above potential energy as

$$\begin{aligned}\Pi_h^{FEM}(\boldsymbol{\rho}_1,\ldots,\boldsymbol{\rho}_m,\boldsymbol{\gamma},\boldsymbol{v}_h) = \sum_{E^{(e)}\in\Omega_h}\Bigg\{ &\sum_{i=1}^{m}\Big[w_i(\overline{\rho}_1^{(e)},\ldots,\overline{\rho}_m^{(e)})\sum_{Q=1}^{N_{E^{(e)}}^Q} w_{E^{(e)}}^Q W_i\Big(\mathbf{C}(\gamma^{(e)}\mathbf{v}_h)\Big)|_{\mathbf{X}=\mathbf{X}_{E^{(e)}}^Q}\Big] \\ &+\Big(1-(\gamma^{(e)})^2\Big)\sum_{Q=1}^{N_{E^{(e)}}^Q} w_{E^{(e)}}^Q W^{L,\rho}\Big(\rho_1^{(e)},\ldots,\rho_m^{(e)},\mathbf{v}_h\Big)|_{\mathbf{X}=\mathbf{X}_{E^{(e)}}^Q}\Bigg\} - \langle\mathbf{t},\mathbf{v}_h\rangle_h. \end{aligned} \tag{89}$$

References

[1] M.P. Bendsøe, A. Klarbring, Joakim Petersson 1968–2002, Struct. Multidiscip. Optim. 25 (3) (2003) 151–152.
[2] O. Sigmund, J. Petersson, Numerical instabilities in topology optimization: a survey on procedures dealing with checkerboards, mesh-dependencies and local minima, Struct. Optim. 16 (1) (1998) 68–75.
[3] T. Borrvall, J. Petersson, Topology optimization using regularized intermediate density control, Comput. Methods Appl. Mech. Engrg. 190 (37–38) (2001) 4911–4928.
[4] T. Borrvall, J. Petersson, Topology optimization of fluids in stokes flow, Internat. J. Numer. Methods Fluids 41 (1) (2003) 77–107.
[5] J. Stegmann, E. Lund, Discrete material optimization of general composite shell structures, Internat. J. Numer. Methods Engrg. 62 (14) (2005) 2009–2027.
[6] F. Wang, B.S. Lazarov, O. Sigmund, J.S. Jensen, Interpolation scheme for fictitious domain techniques and topology optimization of finite strain elastic problems, Comput. Methods Appl. Mech. Engrg. 276 (2014) 453–472.
[7] X.S. Zhang, G.H. Paulino, A.S. Ramos, Multi-material topology optimization with multiple volume constraints: a general approach applied to ground structures with material nonlinearity, Struct. Multidiscip. Optim. 57 (1) (2018) 161–182.
[8] J. Petersson, A finite element analysis of optimal variable thickness sheets, SIAM J. Numer. Anal. 36 (6) (1999) 1759–1778.
[9] T. Borrvall, J. Petersson, Large-scale topology optimization in 3d using parallel computing, Comput. Methods Appl. Mech. Engrg. 190 (46–47) (2001) 6201–6229.
[10] O. Sigmund, S. Torquato, Design of materials with extreme thermal expansion using a three-phase topology optimization method, J. Mech. Phys. Solids 45 (6) (1997) 1037–1067.
[11] L.V. Gibiansky, O. Sigmund, Multiphase composites with extremal bulk modulus, J. Mech. Phys. Solids 48 (3) (2000) 461–498.
[12] C.F. Hvejsel, E. Lund, Material interpolation schemes for unified topology and multi-material optimization, Struct. Multidiscip. Optim. 43 (6) (2011) 811–825.
[13] A.T. Gaynor, N.A. Meisel, C.B. Williams, J.K. Guest, Multiple-material topology optimization of compliant mechanisms created via polyjet three-dimensional printing, J. Manuf. Sci. Eng. 136 (6) (2014) 061015.
[14] A.H. Taheri, K. Suresh, An isogeometric approach to topology optimization of multi-material and functionally graded structures, Internat. J. Numer. Methods Engrg. 109 (5) (2017) 668–696.
[15] E.D. Sanders, M.A. Aguiló, G.H. Paulino, Multi-material continuum topology optimization with arbitrary volume and mass constraints, Comput. Methods Appl. Mech. Engrg. 340 (2018) 798–823.
[16] F. Regazzoni, N. Parolini, M. Verani, Topology optimization of multiple anisotropic materials, with application to self-assembling diblock copolymers, Comput. Methods Appl. Mech. Engrg. 338 (2018) 562–596.
[17] M.Y. Wang, X. Wang, Color level sets: a multi-phase method for structural topology optimization with multiple materials, Comput. Methods Appl. Mech. Engrg. 193 (6) (2004) 469–496.
[18] M.Y. Wang, X. Wang, A level-set based variational method for design and optimization of heterogeneous objects, Comput. Aided Des. 37 (3) (2005) 321–337.
[19] M.Y. Wang, S. Chen, X. Wang, Y. Mei, Design of multimaterial compliant mechanisms using level-set methods, J. Mech. Des. 127 (5) (2005) 941–956.
[20] Y. Mei, X. Wang, A level set method for structural topology optimization with multi-constraints and multi-materials, Acta Mech. Sinica 20 (5) (2004) 507–518.
[21] Y. Wang, Z. Luo, Z. Kang, N. Zhang, A multi-material level set-based topology and shape optimization method, Comput. Methods Appl. Mech. Engrg. 283 (2015) 1570–1586.
[22] M. Wallin, N. Ivarsson, M. Ristinmaa, Large strain phase-field-based multi-material topology optimization, Internat. J. Numer. Methods Engrg. 104 (9) (2015) 887–904.
[23] S. Zhou, M.Y. Wang, Multimaterial structural topology optimization with a generalized Cahn–Hilliard model of multiphase transition, Struct. Multidiscip. Optim. 33 (2) (2007) 89–111.
[24] R. Tavakoli, S.M. Mohseni, Alternating active-phase algorithm for multimaterial topology optimization problems: a 115-line matlab implementation, Struct. Multidiscip. Optim. 49 (4) (2014) 621–642.
[25] W. Zhang, J. Song, J. Zhou, Z. Du, Y. Zhu, Z. Sun, X. Guo, Topology optimization with multiple materials via moving morphable component (MMC) method, Internat. J. Numer. Methods Engrg. 113 (11) (2018) 1653–1675.
[26] X.S. Zhang, G.H. Paulino, A.S. Ramos Jr., Multi-material topology optimization with multiple volume constraints: Combining the zpr update with a ground structure algorithm to select a single material per overlapping set, Int. J. Numer. Methods Eng. 114 (2018) 1053–1073.
[27] G. Zhang, K. Khandelwal, Design of dissipative multimaterial viscoelastic-hyperelastic systems at finite strains via topology optimization, Internat. J. Numer. Methods Engrg. (2019).
[28] M.P. Bendsøe, O. Sigmund, Material interpolation schemes in topology optimization, Arch. Appl. Mech. 69 (9–10) (1999) 635–654.
[29] R.W. Ogden, Non-Linear Elastic Deformations, Dover Publications Inc, Mineola, 1984.
[30] T. Buhl, C. Pedersen, O. Sigmund, Stiffness design of geometrically nonlinear structures using topology optimization, Struct. Multidiscip. Optim. 19 (2) (2000) 93–104.
[31] G. Yoon, Y.Y. Kim, Element connectivity parameterization for topology optimization of geometrically nonlinear structures, Int. J. Solids Struct. 42 (7) (2005) 1983–2009.
[32] R.D. Lahuerta, E.T. Simões, E.M. Campello, P.M. Pimenta, E.C. Silva, Towards the stabilization of the low density elements in topology optimization with large deformation, Comput. Mech. 52 (4) (2013) 779–797.
[33] N. van Dijk, M. Langelaar, F. van Keulen, Element deformation scaling for robust geometrically nonlinear analyses in topology optimization, Struct. Multidiscip. Optim. 50 (4) (2014) 537–560.

[34] Y. Luo, M.Y. Wang, Z. Kang, Topology optimization of geometrically nonlinear structures based on an additive hyperelasticity technique, Comput. Methods Appl. Mech. Engrg. 286 (2015) 422–441.
[35] Q. Luo, L. Tong, An algorithm for eradicating the effects of void elements on structural topology optimization for nonlinear compliance, Struct. Multidiscip. Optim. 53 (4) (2016) 695–714.
[36] S. Wang, E. de Sturler, G.H. Paulino, Dynamic adaptive mesh refinement for topology optimization, 2010, arXiv preprint arXiv:1009.4975.
[37] M. Bruggi, M. Verani, A fully adaptive topology optimization algorithm with goal-oriented error control, Comput. Struct. 89 (15–16) (2011) 1481–1493.
[38] Y.-Q. Wang, J.-J. He, Z. Luo, Z. Kang, An adaptive method for high-resolution topology design, Acta Mech. Sinica 29 (6) (2013) 840–850.
[39] H. Nguyen-Xuan, A polytree-based adaptive polygonal finite element method for topology optimization, Int. J. Numer. Methods Eng. 110 (10) (2017) 972–1000.
[40] T.W. Chin, G.J. Kennedy, Multimaterial thermoelastic stress-constrained topology optimization of structures with adaptive mesh refinement, in: 2018 Multidisciplinary Analysis and Optimization Conference, AIAA Aviation 2018, 2018, AIAA 2018-4054.
[41] K.N. Chau, K.N. Chau, T. Ngo, K. Hackl, H. Nguyen-Xuan, A polytree-based adaptive polygonal finite element method for multi-material topology optimization, Comput. Methods Appl. Mech. Engrg. 332 (2018) 712–739.
[42] L. Beirão da Veiga, F. Brezzi, L.D. Marini, Virtual elements for linear elasticity problems, SIAM J. Numer. Anal. 51 (2) (2013) 794–812.
[43] A.L. Gain, C. Talischi, G. Paulino, On the virtual element method for three-dimensional linear elasticity problems on arbitrary polyhedral meshes, Comput. Methods Appl. Mech. Engrg. 282 (2014) 132–160.
[44] E. Artioli, S. De Miranda, C. Lovadina, L. Patruno, A stress/displacement Virtual Element method for plane elasticity problems, Comput. Methods Appl. Mech. Engrg. 325 (2017) 155–174.
[45] M. Mengolini, M.F. Benedetto, A.M. Aragón, An engineering perspective to the virtual element method and its interplay with the standard finite element method, Comput. Methods Appl. Mech. Engrg. (2019).
[46] L. Beirão da Veiga, C. Lovadina, D. Mora, A virtual element method for elastic and inelastic problems on polytope meshes, Comput. Methods Appl. Mech. Engrg. 295 (2015) 327–346, 10.
[47] E. Artioli, L. Beirão da Veiga, C. Lovadina, E. Sacco, Arbitrary order 2D virtual elements for polygonal meshes: Part I, elastic problem, Comput. Mech. 60 (2017) 355–377.
[48] E. Artioli, L. Beirão da Veiga, C. Lovadina, E. Sacco, Arbitrary order 2D virtual elements for polygonal meshes: part II, inelastic problem, Comput. Mech. 60 (2017) 643–657.
[49] R.L. Taylor, E. Artioli, Vem for Inelastic Solids, in Advances in Computational Plasticity: A Book in Honour of D. Roger J. Owen, Springer, Cham, 2018, pp. 381–394,
[50] H. Chi, L. Beirão da Veiga, G. Paulino, Some basic formulations of the virtual element method (VEM) for finite deformations, Comput. Methods Appl. Mech. Engrg. 318 (2017) 148–192.
[51] P. Wriggers, B. Reddy, W. Rust, B. Hudobivnik, Efficient virtual element formulations for compressible and incompressible finite deformations, Comput. Mech. 60 (2017) 253–268.
[52] P. Wriggers, B. Hudobivnik, A low order virtual element formulation for finite elasto-plastic deformations, Comput. Methods Appl. Mech. Engrg. 327 (2017) 459–477.
[53] F. Brezzi, L.D. Marini, Virtual Element Methods for plate bending problems, Comput. Methods Appl. Mech. Engrg. 253 (2013) 455–462.
[54] P. Antonietti, G. Manzini, M. Verani, The fully nonconforming virtual element method for biharmonic problems, 23, (2) 2018, pp. 387–407,
[55] D. Mora, G. Rivera, I. Velásquez, A virtual element method for the vibration problem of kirchhoff plates, 52, (4) 2018, pp. 1437–1456,
[56] J. Zhao, S. Chen, B. Zhang, The nonconforming virtual element method for plate bending problems, Math. Models Methods Appl. Sci. 26 (09) (2016) 1671–1687.
[57] P. Wriggers, W. Rust, B. Reddy, A virtual element method for contact, Comput. Mech. 58 (2016) 1039–1050, 12.
[58] F. Aldakheel, B. Hudobivnik, A. Hussein, P. Wriggers, Phase-field modeling of brittle fracture using an efficient virtual element scheme, Comput. Methods Appl. Mech. Engrg. 341 (2018) 443–466.
[59] M.F. Benedetto, A. Caggiano, G. Etse, Virtual elements and zero thickness interface-based approach for fracture analysis of heterogeneous materials, Comput. Methods Appl. Mech. Engrg. 338 (2018) 41–67.
[60] A.L. Gain, G.H. Paulino, L.S. Duarte, I.F. Menezes, Topology optimization using polytopes, Comput. Methods Appl. Mech. Engrg. 293 (2015) 411–430.
[61] P.F. Antonietti, M. Bruggi, S. Scacchi, M. Verani, On the virtual element method for topology optimization on polygonal meshes: a numerical study, Comput. Math. Appl. 74 (5) (2017) 1091–1109.
[62] H. Chi, A. Pereira, I.F. Menezes, G.H. Paulino, Virtual element method (vem)-based topology optimization: an integrated framework, Struct. Multidiscip. Optim. (2019) 1–26.
[63] X. Zhang, H. Chi, Efficient multi-material continuum topology optimization considering hyperelasticity: achieving local feature control through regional constraints, Mech. Res. Commun. 105 (2020) 103494.
[64] M.P. Bendsøe, O. Sigmund, Topology Optimization: Theory, Methods, and Applications, Springer, Berlin, Germany, 2003.
[65] K. Svanberg, The method of moving asymptotes – a new method for structural optimization, Internat. J. Numer. Methods Engrg. 24 (2) (1987) 359–373.

[66] M. Cui, H. Chen, An improved alternating active-phase algorithm for multi-material topology optimization problems, in: Applied Mechanics and Materials, vol. 635, Trans Tech Publ, 2014, pp. 105–111.
[67] J. Park, A. Sutradhar, A multi-resolution method for 3D multi-material topology optimization, Comput. Methods Appl. Mech. Engrg. 285 (2015) 571–586.
[68] E.D. Sanders, A. Pereira, M.A. Aguiló, G.H. Paulino, Polymat: an efficient matlab code for multi-material topology optimization, Struct. Multidiscip. Optim. 58 (6) (2018) 2727–2759.
[69] J. Bonet, R.D. Wood, Nonlinear Continuum Mechanics for Finite Element Analysis, Cambridge University Press, 2008.
[70] A. Klarbring, N. Strömberg, Topology optimization of hyperelastic bodies including non-zero prescribed displacements, Struct. Multidiscip. Optim. 47 (1) (2013) 37–48.
[71] R.W. Ogden, Large deformation isotropic elasticity–on the correlation of theory and experiment for incompressible rubberlike solids, Proc. R. Soc. Lond. Ser. A Math. Phys. Eng. Sci. 326 (1567) (1972) 565–584.
[72] K.M. Moerman, C.K. Simms, T. Nagel, Control of tension–compression asymmetry in Ogden hyperelasticity with application to soft tissue modelling, J. Mech. Behav. Biomed. Mater. 56 (2016) 218–228.
[73] X. Zhang, A.S. Ramos Jr., G.H. Paulino, Material nonlinear topology design using the ground structure method with a discrete filter scheme, Struct. Multidiscip. Optim. 55 (6) (2017) 2045–2072.
[74] O. Lopez-Pamies, M.I. Idiart, An exact result for the macroscopic response of porous Neo-Hookean solids, J. Elasticity 95 (1–2) (2009) 99.
[75] L. Beirão da Veiga, F. Brezzi, A. Cangiani, G. Manzini, L.D. Marini, A. Russo, Basic principles of virtual element methods., Math. Models Methods Appl. Sci. 23 (1) (2013) 199–214.
[76] P. Wriggers, Nonlinear Finite Element Methods, Springer Science & Business Media, 2008.
[77] B. Bourdin, Filters in topology optimization, Internat. J. Numer. Methods Engrg. 50 (9) (2001) 2143–2158.
[78] C. Talischi, G.H. Paulino, A. Pereira, I.F.M. Menezes, PolyTop: a Matlab implementation of a general topology optimization framework using unstructured polygonal finite element meshes, Struct. Multidiscip. Optim. 45 (2012) 329–357.
[79] T.J.R. Hughes, The Finite Element Method: Linear Static and Dynamic Finite Element Analysis, Courier Dover Publications, 2012.
[80] R. Haftka, M. Kamat, Simultaneous nonlinear structural analysis and design, Comput. Mech. 4 (6) (1989) 409–416.
[81] A. Klarbring, N. Strömberg, A note on the min–max formulation of stiffness optimization including non-zero prescribed displacements, Struct. Multidiscip. Optim. 45 (2012) 147–149, 1.
[82] A.S. Ramos Jr., G.H. Paulino, Convex topology optimization for hyperelastic trusses based on the ground-structure approach, Struct. Multidiscip. Optim. 51 (2) (2015) 287–304.
[83] O. Sigmund, On the design of compliant mechanisms using topology optimization, J. Struct. Mech. 25 (4) (1997) 493–524.
[84] T.E. Bruns, D.A. Tortorelli, Topology optimization of non-linear elastic structures and compliant mechanisms, Comput. Methods Appl. Mech. Engrg. 190 (26–27) (2001) 3443–3459.
[85] C.B. Pedersen, T. Buhl, O. Sigmund, Topology synthesis of large-displacement compliant mechanisms, Int. J. Numer. Methods Eng. 50 (12) (2001) 2683–2705.
[86] Z. Ma, N. Kikuchi, I. Hagiwara, Structural topology and shape optimization for a frequency response problem, Comput. Mech. 13 (3) (1993) 157–174.
[87] H. Chi, L. Beirão da Veiga, G.H. Paulino, A simple and effective gradient recovery scheme and a posteriori error estimator for the Virtual Element Method (VEM), Comput. Methods Appl. Mech. Engrg. 347 (2019) 21–58.
[88] S.E. Leon, E.N. Lages, C.N. de Araújo, G.H. Paulino, On the effect of constraint parameters on the generalized displacement control method, Mech. Res. Commun. 56 (2014) 123–129.
[89] X.S. Zhang, E. de Sturler, G.H. Paulino, Stochastic sampling for deterministic structural topology optimization with many load cases: Density-based and ground structure approaches, Comput. Methods Appl. Mech. Engrg. 325 (2017) 463–487.
[90] F. Wang, B.S. Lazarov, O. Sigmund, On projection methods, convergence and robust formulations in topology optimization, Struct. Multidiscip. Optim. 43 (6) (2011) 767–784.
[91] H. Chi, C. Talischi, O. Lopez-Pamies, G.H. Paulino, A paradigm for higher order polygonal elements in finite elasticity, Comput. Methods Appl. Mech. Engrg. 306 (2016) 216–251.